Sustainable Cities and Society 149 (2026) 107804

Contents lists available at ScienceDirect

Sustainable Cities and Society

journal homepage: www.elsevier.com/locate/scs

Wind direction shapes spatial cooling distribution of urban canals: Large-eddy simulation of turbulent and advective heat transport with PALM4U in Amsterdam☆

Xuan Chen [a,*], Srinidhi Gadde [b], Gert-Jan Steeneveld [c], Remko Uijlenhoet [a]

[a] Department of Water Management, Faculty of Civil Engineering and Geoscience, Delft University of Technology, Delft, 2628 CD, The Netherlands
[b] Department of Geosciences, Faculty of Geo-information Science and Earth Observation (ITC), University of Twente, Enschede, 7522 NB, The Netherlands
[c] Meteorology and Air Quality Section, Wageningen University, Wageningen, P.O. box 47, 6700 AA, The Netherlands

ARTICLE INFO

Keywords:
Urban water cooling
Nature-based heat mitigation
Advection cooling
Multi-physics LES
WRF-PALM

ABSTRACT

Urban water bodies offer nature-based heat mitigation solutions, yet the mechanistic contributions of turbulent exchange versus advective transport in redistributing canal-induced cooling remain unquantified. We employed PALM4U large-eddy simulation with realistic urban geometry to investigate canal cooling mechanisms in Amsterdam, Netherlands, a dense historic center whose semi-circular canal ring enables systematic study of varying wind-canal orientations within a single setting. Model evaluation against eddy covariance and urban weather station observations demonstrated strong performance for sensible heat flux, net radiation, and near-surface air temperature. Through controlled experiments, we decomposed cooling into turbulent and advective components, revealing that effectiveness depends fundamentally on wind-canal orientation. When wind flows perpendicular to canals, mechanically-driven canyon vortices redistribute cool air from the water surface to surrounding areas, with advection accounting for 60 to 80% of the total cooling effect over adjacent pavement and above the canopy, extending cooling asymmetrically to 2 to 3 building heights vertically and into adjacent canyons. When wind flows parallel to canals, the absence of a cross-canyon vortex limits redistribution, leaving cooling concentrated near the water surface and driven predominantly by local sensible heat flux reduction. Wind-canal orientation does not markedly alter overall cooling intensity but governs how cooling is spatially redistributed within the canopy, producing pronounced thermal heterogeneity, with temperature differences up to 1.5 °C within individual street canyons. While these magnitudes reflect a single summer day and Amsterdam's specific morphology, the mechanism points to a transferable principle: orienting blue infrastructure relative to prevailing summer winds can steer cooling toward pedestrian spaces.

1. Introduction

Cities worldwide face increasing heat stress from urbanization and climate change (Geletič et al., 2023; Lorenz et al., 2019; Wouters et al., 2017). To counteract urban heat stress, small urban water bodies, like fountains, ponds, and canals, have emerged as a nature-based solution (Chen et al., 2024; Kumar et al., 2024; Yao et al., 2023). Small urban water surfaces can cool urban environments during daytime through mechanisms such as evaporative cooling and reduced sensible heat flux, due to their lower surface temperatures relative to built surfaces, and the possible generation of horizontal advection of cooler air away from the water body, which may redistribute heat across the urban canopy (Ampatzidis & Kershaw, 2020; Chen et al., 2026). Yet, the relative importance of vertical turbulent exchange and horizontal advective transport remains context-dependent and is not yet well understood, leaving open questions about the magnitude and spatial reach of these cooling effects in urban street canyons (Chen et al., 2026).

Investigating the thermal effects of small urban water bodies requires microscale resolution capable of capturing the thermal and flow heterogeneity within street canyons (Toparlar et al., 2017). The characteristic scales of building-water interactions demand models that resolve both individual buildings and water bodies explicitly (Guo et al.,

☆ This work is supported by the 4TU program HERITAGE (HEat Robustness in Relation To AGEing cities), funded by the High Tech for a Sustainable Future (HTSF) program of 4TU, the federation of the four technical universities in the Netherlands. This work used the Dutch national e-infrastructure with the support of the SURF Cooperative, using grant no. EINF-2023.042. The observations have been supported by Amsterdam Institute for Advanced Metropolitan Solutions (AMS Institute, project VIR16002), and the Dutch Research Council (NWO) Project 864.14.007.

* Corresponding author.
E-mail address: x.chen-12@tudelft.nl (X. Chen).

https://doi.org/10.1016/j.scs.2026.107804
Received 17 March 2026; Received in revised form 6 August 2026; Accepted 7 August 2026
Available online 28 August 2026

2023). Several microscale studies have investigated urban water body cooling effects using computational fluid dynamics approaches. Tominaga et al. (2015) applied CFD simulations to assess evaporative cooling effects from water surfaces in residential neighborhoods, reporting approximately 2.0°C air temperature decrease at pedestrian level with cooling effects propagating up to 100 m downwind. Jacobs et al. (2020) used ENVI-met model to evaluate thermal effects of typical Dutch urban water bodies, finding afternoon air temperature reductions of 0.2 to 0.6°C in surrounding spaces. Wang et al. (2025) employed CFD simulations validated against field measurements to examine water body evaporation modeling and microclimate cooling effects. While these studies provide valuable insights into spatial cooling patterns and the relative reduction of 2-m air temperature, they are context-dependent and do not investigate the underlying mechanisms, especially vertical and horizontal advection of turbulent fluxes. Furthermore, they rely on Reynolds-Averaged Navier–Stokes (RANS) simulations, which completely parameterize turbulence and utilize time-averaged flow equations, eliminating the intermittent fluctuations essential to turbulent transport (Salim et al., 2011). This simplification introduces uncertainties in turbulence modeling and fundamentally limits physical accuracy for advective processes. For example, Tominaga et al. (2015) reported cooling propagating up to 100 m downwind, a signature of advective transport. However, because the cooling appears only as a downwind temperature gradient, the advective contribution is not isolated or quantified and the RANS framework cannot resolve the turbulent eddies that govern this transport.

Previous microscale studies focus predominantly on air temperature for both evaluation and analysis (Ampatzidis & Kershaw, 2020; Manteghi et al., 2015). While these assessments show localized cooling near water surfaces, they reveal little about the physical mechanisms driving heat redistribution (Amaripadath & Sailor, 2025; Crank et al., 2018). The surface energy partitioning, which is the actual pathway regulating surface-atmosphere energy exchange (Crawford et al., 2017; Offerle et al., 2007), remains largely unquantified. More critically, horizontal microscale advective heat transport is rarely explicitly quantified, despite likely being a dominant mechanism for propagating cooling downwind (Chen et al., 2026). Although several CFD studies show downwind cooling dispersion in their temperature fields, these effects remain implicitly embedded in mean temperature distributions rather than being decomposed and analyzed as a distinct transport pathway. Thus, the novelty of the current study lies not in identifying advective cooling but in explicitly resolving, decomposing, and comparing the turbulent and advective pathways within a turbulence-resolving framework. Recent systematic reviews of urban cooling methodologies confirm this predominant focus on temperature metrics rather than underlying energy transport processes (Galalizadeh et al., 2024). This gap limits our ability to predict cooling effectiveness under varying conditions at the neighborhood scale. The turbulent sensible heat flux determines whether water bodies reduce total heat input to the urban boundary layer or redistribute existing heat, while horizontal advective heat transport governs how thermal benefits extend and controls their spatial propagation. Key questions remain: How do urban water bodies modify turbulent heat exchange, which is predominantly vertical against horizontal advective transport? What are the relative magnitudes of these pathways? What flow structures facilitate heat transport away from water surfaces?

To investigate these questions, large-eddy simulation (LES) is required to explicitly resolve large energy-containing turbulent eddies on the order of the grid size (Gadde et al., 2021). This capability enables direct computation of both vertical turbulent heat exchange and horizontal advective transport from resolved scale motions. For urban water body applications, LES can capture the three-dimensional turbulent eddy structures that govern heat transport in complex building-canal configurations (Anders et al., 2023). The ability to resolve turbulent fluctuations is essential for quantifying horizontal advective heat fluxes, which depend on transient thermal circulations and intermittent flow structures.

The current study employs the PALM for Urban applications large-eddy simulation (PALM4U LES) system (Maronga et al., 2020) to address these knowledge gaps using Amsterdam's canal network as a case study. Amsterdam's extensive canal system, embedded within dense historic building arrays, provides a representative environment for investigating the effects of narrow urban water bodies on heat transport. We pursue two objectives. First, we evaluate PALM4U LES performance for a realistic Amsterdam case by assessing model accuracy of near-surface meteorology and surface-atmosphere heat exchange against eddy covariance (EC) tower and urban weather station observations (Jansen et al., 2023; Ronda et al., 2017; van der Meer et al., 2025) (Section 3). Second, we characterize canal-induced flow structures and quantify their impacts on heat exchange by analyzing mean flow patterns and thermal circulations in a realistic canal environment (Section 4), isolating canal-induced modifications to sensible heat flux partitioning and explicitly decomposing and quantifying the relative magnitudes of vertical turbulent exchange versus horizontal advective transport that prior temperature-based and RANS studies could not provide (Chen et al., 2026) (Section 5).

2. Methodology and materials

2.1. Study area

The study focuses on Amsterdam, The Netherlands (52.37°N, 4.90°E), which features a temperate oceanic climate (Köppen classification, Cfb). Amsterdam is an archetypal canal city with approximately 165 canals comprising roughly 25% of the historic center's surface area (UNESCO World Heritage Centre, 2010). This centuries-old water network, originally designed for transportation and water management during the 17th century, is now tightly integrated within dense building arrays that characterize the historic city center. The canal widths typically range from 15 to 30 m (Figs. 1c, 5b and d) and canals are embedded within complex building configurations that create flow channeling and blocking effects. These geometric characteristics make Amsterdam well-suited for examining how urban canals partition their cooling effect between vertical turbulent heat exchange and horizontal advective transport. Furthermore, Amsterdam's concentric semi-circular canal layout naturally presents a continuous spectrum of wind–canal orientation configurations within a single simulation domain, enabling comparative analysis of orientation effects without requiring multiple separate model runs or land-use scenarios.

2.2. Mesoscale forcing

The modeling framework employs a multi-scale downscaling approach, transitioning from global to mesoscale using the Weather Research and Forecasting (WRF) model (Skamarock et al., 2019), and subsequently from mesoscale to microscale using the PALM4U model. Initial and lateral boundary conditions for WRF were derived from ERA5 global reanalysis data (Hersbach et al., 2020).

The WRF simulation domain configuration is illustrated in Fig. 1a, with the innermost nested domain at 1 km horizontal resolution centered over Amsterdam (Fig. 1b). Simulations spanned four complete diurnal cycles (96 h total), and WRF results were evaluated against meteorological station observations to ensure accurate representation of synoptic-scale atmospheric patterns. Complete details of the WRF model configuration, including domain specifications, physics parameterizations, and vertical discretization, are provided in the Supplementary Material Table S1.

Atmospheric forcing for the PALM4U model was provided through the PALM4U mesoscale nesting interface, which facilitates dynamic coupling between large-scale meteorological fields and the microscale urban simulations. WRF output fields were preprocessed using the

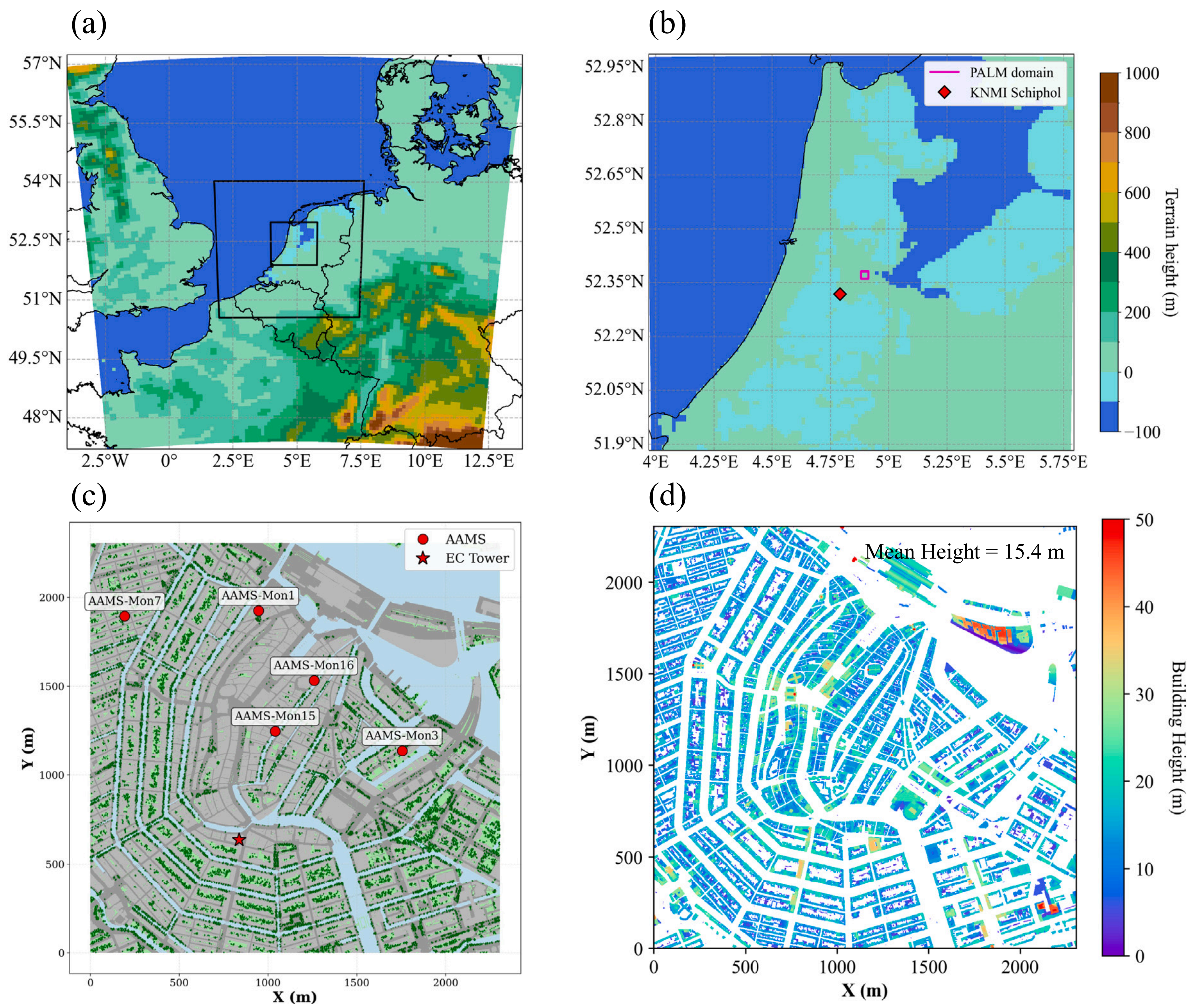

Fig. 1. Illustration of the (a) WRF simulation domains 1 to 3, (b) Innermost WRF nesting domain with the location of the KNMI weather station Schiphol airport use for evaluation of WRF (WMO 06240, red diamond) and PALM4U LES area (violet square), (c) PALM4U LES domain with land use and locations of the EC tower and urban weather stations, (d) building height over the PALM4U LES domain.

Table 1
Numerical and physical parameterization schemes used in PALM4U.

Scheme/Module	Reference
Third-order Runge–Kutta scheme	Williamson (1980)
Fifth-order advection scheme	Wicker and Skamarock (2002)
1.5-order turbulence closure	Deardorff (1980) and Saiki et al. (2000)
Urban Surface Model (USM)	Resler et al. (2017)
Land Surface Model (LSM)	Gehrke et al. (2021)
Plant Canopy Model (PCM)	Krč et al. (2021)
Human Biometeorology Model	Fröhlich and Matzarakis (2020)
Radiative Transfer Model (RTM)	Krč et al. (2021) and Salim et al. (2022)
Rapid Radiative Transfer Model for Global (RRTMG)	Mlawer et al. (1997) and Iacono et al. (2008)

PALM-meteo utility (Krč et al., 2025), which interpolates and transforms mesoscale data into the dynamic driver format required by PALM. This approach ensures physically consistent, realistic time-varying boundary conditions that capture the evolution of synoptic weather patterns throughout the simulation period. LES covered a 24-hour period (Aug 13, 2022) extracted from the 96-hour WRF simulation window.

2.3. PALM4U LES model configurations

PALM4U model system version 23.04 is applied in the current study (Maronga et al., 2020). The model resolves the incompressible, non-hydrostatic, Navier–Stokes equations governing momentum, heat, and moisture transport under the Boussinesq approximation. The numerical framework is based on a staggered Arakawa C grid structure in three-dimensional Cartesian coordinates. To address urban microclimate processes, the PALM4U model contains an explicit representation of complex urban building configurations directly on the computational mesh with specialized parameterizations. The model includes fully coupled urban surface energy balance schemes for roofs, walls, and roads; a land surface model that resolves soil heat transfer, vegetation processes, and water surface; and a radiative transfer module accounting for shortwave and longwave interactions, including canyon shading and reflections. Moisture processes, including evaporation and latent heat fluxes, are also represented. A complete list of numerical and physical parameterization schemes used in this study is provided in

Table 2
Configuration of LES domain.

Horizontal grid size	8 m and 2 m
Vertical grid size	8 m and 2 m at the first grid level
Grid points	768 × 768 × 144 and 1152 × 1152 × 144

Table 1. Further technical details of the PALM4U modeling system are provided in Maronga et al. (2020, 2015). The dynamic core of PALM4U has been evaluated against wind tunnel experiments in a neutrally stratified urban environment, demonstrating its ability to reproduce canyon vorticity structures and turbulent flow regimes (Gronemeier et al., 2021).

The LES implementation utilized a two-way nested domain configuration consisting of an outer parent domain and an inner child domain, with horizontal resolutions of 8 m and 2 m, respectively (Table 2). The 2 m horizontal resolution corresponds to approximately 7–15 grid points across typical canal widths within our simulation domain, which is sufficient to resolve neighborhood-scale heat transport mechanisms from the canal to nearby streets and buildings (Hollósi et al., 2024; Vogel et al., 2022).

In the vertical direction, both domains used 144 grid levels. The outer domain employed a uniform vertical grid spacing of 8 m from the surface to 512 m, above which grid stretching was applied with a stretching factor of 1.08, yielding a maximum vertical spacing of 20 m near the domain top. The inner child domain maintained uniform vertical grid spacing of 2 m throughout the entire vertical extent, adequately resolving the urban canopy layer (mean building height ~15 m, Fig. 1d). This nested approach allows for progressive refinement of turbulent structures while maintaining computational efficiency, with the inner domain (2.3 km × 2.3 km, Fig. 1c) positioned to cover the heritage city center of Amsterdam.

To verify that the 2 m resolution of the nested domain adequately captures the vorticity structures, two idealized sensitivity simulations were conducted at 2 m and 1 m horizontal and vertical resolution under identical meteorological conditions, with wind forced perpendicular to the canyon and canal axis. The idealized simulations use the same configuration and setup as the main numerical experiment (Section 2.5), differing only in the idealized landscape layout, which fixes the street–wind orientation to isolate the vortex structure. The idealized domain is shown in Figure S1b. The average daytime 2-m air temperature differs by 0.1 K between the two resolutions. Figures S2a and S2b compare the spanwise vorticity fields at a vertical cross-section for the 2 m and 1 m runs at noon. Quantitatively, the two fields agree closely, with a coefficient of determination of 0.95 and a mean absolute difference of 2.5% relative to the average vorticity magnitude. These results indicate that the 2 m resolution adequately resolves the essential vorticity structures and circulation patterns, and that further grid refinement yields only marginal improvements in the dominant flow features relevant to urban heat transport.

2.4. Urban geometric inputs

The PALM4U urban modules require land surface classification, three dimensional urban geometry, vegetation structure, and material properties as model inputs. Fig. 1c shows the land surface classification over the child simulation domain. Land surface types were classified using Basisregistratie Grootschalige Topografie (PDOK, 2025b), the official large-scale topographic register documenting all physical features, including buildings, roads, water bodies, railways, and agricultural land. Building footprints were sourced from Basisregistratie Adressen en Gebouwen (PDOK, 2025a), the national building registry containing structural attributes such as footprint area, construction year, and function.

Building geometry was derived from 3DBAG (Peters et al., 2022), a nationwide dataset containing all 10 million buildings in the Netherlands in CityJSON format at LOD2.2 specification. Building heights were extracted from the 3D city model following the approach of Heldens et al. (2020). Fig. 1d shows the spatial map of the building height over the simulation domain, with a mean height of 15.4 m. Terrain elevation was obtained from Actueel Hoogtebestand Nederland (Overheid, 2023), the Dutch national elevation model providing 0.5 m resolution coverage across the country. Vertical coordinates in subsequent analyses are normalized by the mean building height (z/z_H, where z_H = 15.4 m).

Vegetation parameters, including tree locations, stem positions, heights, crown diameters, and trunk sizes, were obtained from the Cobra Groeninzicht municipal database (Cobra-Groeninzicht, 2025). Crown shapes for species identified trees were assigned from PALM4U lookup tables. Leaf area index (LAI) and leaf area density (LAD) were estimated using NDVI-LAI correlations (Wang et al., 2005) following (Heldens et al., 2020), with NDVI calculated from 8 cm resolution color-infrared imagery (PDOK, 2025c). We acknowledge uncertainties in LAI estimates due to the empirical nature of this approach and the absence of direct high-resolution measurements.

Physical and thermal properties for pavements, bare soil, and vegetated surfaces were prescribed from standardized lookup tables integrated within the PALM4U framework (Heldens et al., 2020). In the absence of spatially explicit albedo data, albedo values were specified based on typical Dutch building characteristics: 0.1 for roofs (bituminous materials) and 0.25 for walls (red brick). Window and wall fractions were set to 0.4 and 0.6, respectively, based on average window to wall ratio in Amsterdam derived by Dang et al. (2024) using panoramic images and facade texturing. All input datasets were converted to raster format and processed in accordance with the PALM4U Input Data Standard (PIDS).

2.5. Numerical experiments and setup

To quantify the thermal impact of Amsterdam's canal network, two contrasting simulations were performed. The reference case (CTRL) incorporates the actual urban morphology including all canal water bodies, while the modified case (NOWAT) replaces all canal surfaces with the impervious pavement type of the immediately surrounding streets, preserving all other urban geometry and surface characteristics unchanged (Supplementary Material Fig. S4). In PALM4U land-surface model, each land-use type is characterized by a distinct and internally consistent set of surface parameters including aerodynamic roughness, albedo, emissivity, thermal properties, and surface energy balance formulation (Gehrke et al., 2021). Consequently, the CTRL–NOWAT difference captures the full, physically coupled microclimate effect of canal presence, reflecting the integrated contrast between the radiative, thermal, and turbulent exchange properties of open water and impervious pavement as they co-exist in the real urban environment.

Water surfaces in PALM4U are identified through the water type variable in the static input file, which classifies water bodies into five categories (lakes, rivers, oceans, ponds, and fountains) with type-specific roughness lengths and thermal properties. Here, the canals are set as the river type. The land surface model employs a simplified skin-layer energy balance approach where water surfaces are assigned a very high thermal conductivity ($\lambda = 1 \times 10^{10}$ W m^{-1} K^{-1}) that effectively forces the surface temperature to match the prescribed subsurface value. This formulation computes sensible and latent heat fluxes without prognostic temperature evolution, explicit shortwave penetration, water column stratification, or sediment heat exchange (Gehrke et al., 2021). For both CTRL and NOWAT simulations, canal water temperature was held constant at 295 K throughout the 24-hour period, based on typical summer surface water temperatures from the Dutch national water monitoring network. Observations at nearby monitoring stations on August 13, 2022, showed minimal diurnal variation (standard deviation 0.27°C), justifying the constant temperature assumption for this single-day simulation given the large thermal mass of canal water relative to atmospheric forcing (Rijkswaterstaat, 2022).

To assess the sensitivity of the results to this assumption, two additional simulations were conducted with water temperature prescribed at 294 K and 296 K, representing plausible uncertainty around the baseline value.

Full diurnal cycle simulations were conducted for August 13, 2022 (00:00 UTC to August 13 00:00 UTC), a summer day selected from the middle of the WRF simulation period. Meteorological conditions at Amsterdam Schiphol airport were characterized by a high-pressure system (1015.5 hPa) with no nearby frontal activity, nearly clear skies (solar radiation peaking at 800 W m^{-2}), light easterly winds (mean 2.5 m s^{-1}), and no precipitation. Temperature ranged from 16.8°C (morning, minimum) to 30.5°C (afternoon, maximum), representing typical north-west European summer anticyclonic weather (KNMI, 2022). The selection of a normal summer day, rather than an extreme event, is intentional: our research questions focus on understanding the fundamental mechanisms by which urban water bodies modify heat transport, specifically the balance between vertical turbulent exchange and horizontal advection. These mechanistic processes are most clearly isolated under typical conditions where local urban surface effects dominate over synoptic-scale forcing, whereas extreme heatwave events involve anomalous large-scale patterns that can mask local effects (Liu et al., 2020; Stefanon et al., 2012).

To ensure physically consistent initial conditions, a two-stage spin-up approach was adopted. First, a 24-hour thermal spin-up was performed prior to activating the 3D atmospheric simulation, during which LSM and USM were run without an interactive atmosphere (Linden et al., 2023; Maronga et al., 2020). During this phase, soil and wall layer temperatures were allowed to equilibrate under prescribed radiation forcing and a diurnal near-surface air temperature cycle, ensuring that surface energy partitioning at simulation start reflects a realistic thermal state. Subsequently, once the 3D atmospheric code was activated, the first two hours of each simulation were excluded from analysis, exceeding two flow-through times across the 2.3 km domain, to ensure fully developed turbulence fields and canyon-scale circulations prior to any diagnostic sampling. Domain-averaged temperature, sensible heat flux, and advective heat flux had reached a quasi-stable state after the 24-hour thermal spin-up and by the end of the first two hours of the simulation period.

2.6. Observations

Model evaluation was conducted using observational data from three complementary monitoring systems: a meteorological station at Schiphol airport for mesoscale simulation evaluation; a network of urban weather stations distributed across the Amsterdam metropolitan area; and an EC flux tower in central Amsterdam.

Regional meteorological conditions were obtained from the Royal Netherlands Meteorological Institute (KNMI) weather station at Schiphol airport (KNMI Schiphol dataset). This station provides standard hourly observations of air temperature at 2 m, 10 m wind, and incoming shortwave radiation and is located approximately 15 km southwest of Amsterdam's city center (Fig. 1b). The Schiphol station represents background meteorological conditions outside the direct urban influence, providing an evaluation dataset for regional-scale atmospheric forcing simulated by WRF.

Neighborhood-scale meteorological variability was monitored using a network of 25 automated weather stations distributed across Amsterdam (Ronda et al., 2017). Of the 25 stations, 5 are within the LES inner domain (red dots in Fig. 1). These stations, part of the Amsterdam Atmospheric Monitoring Supersite (AAMS), measure air temperature, wind speed, and wind direction at street-canyon level (Amini et al., 2026; Ronda et al., 2017). The stations are strategically positioned to capture spatial variations in the urban microclimate. All sensors are mounted on lampposts at approximately 4 m above ground level. Fig. S3a presents a photo of one of the sensors. The stations record measurements at 10-minute intervals, providing high temporal resolution data for model evaluation. Ronda et al. (2017) demonstrated that this network successfully captures the urban heat island effect in Amsterdam, with mean evening temperature differences of approximately 1.0°C between neighborhoods and maximum differences reaching 4.5°C during summer conditions.

The EC tower measuring turbulent fluxes is located at 52.37°N, 4.89°E in Amsterdam's city center (red star in Fig. 1c), on the rooftop of a building 39.2 m high (van der Meer et al., 2025). Fig. S2b shows the photo of the EC tower. The tower measures turbulent fluxes using a Campbell Scientific CSAT3 sonic anemometer and also coupled with a LICOR Li-7500 open-path gas analyzer. Sensible heat flux measurements are processed using standard eddy covariance methodology with quality control procedures applied following established protocols (Foken et al., 2004; van der Meer et al., 2025). Net radiation components are measured using a four-component radiation system consisting of Kipp & Zonen CM11 pyranometers (upgraded) for incoming and outgoing shortwave radiation, and Kipp & Zonen SGR3 smart pyrgeometers for incoming and outgoing longwave radiation. High frequency data from EC system are processed to obtain continuous half-hourly averaged fluxes and 1-minute radiation measurements, enabling detailed analysis of diurnal and seasonal patterns in urban surface-atmosphere exchange (Jansen et al., 2023).

2.7. Model evaluation metrics

Model performance was quantified using three statistical metrics: root mean square error (RMSE), coefficient of determination (R^2), and index of agreement (IoA) (Willmott et al., 1985). RMSE measures the average magnitude of prediction errors:

$$\mathrm{RMSE} = \sqrt{\frac{1}{n}\sum_{i=1}^{n}(M_i - O_i)^2} \tag{1}$$

where M_i and O_i are the modeled and observed values, respectively, and n is the number of data points. The coefficient of determination (R^2) quantifies the proportion of variance in observations explained by the model:

$$R^2 = 1 - \frac{\sum_{i=1}^{n}(O_i - M_i)^2}{\sum_{i=1}^{n}(O_i - \bar{O})^2} \tag{2}$$

where $\bar{O}$ is the mean of observed values. The index of agreement (IoA) provides a standardized measure of model accuracy:

$$\mathrm{IoA} = 1 - \frac{\sum_{i=1}^{n}(O_i - M_i)^2}{\sum_{i=1}^{n}(|M_i - \bar{O}| + |O_i - \bar{O}|)^2} \tag{3}$$

RMSE has the same units as the evaluated variable and indicates typical prediction error magnitude, with lower values indicating better performance. R^2 ranges from negative infinity to 1, where 1 indicates perfect predictions and values closer to 1 indicate better model performance. IoA ranges from 0 to 1, with 1 representing perfect agreement (Willmott et al., 1985). IoA represents the degree to which model predictions match both the temporal pattern and variability of observed values. It evaluates both the magnitude and direction of deviations relative to the mean of the observations, providing a normalized measure of model performance. These metrics were computed for sensible heat flux, air temperature, wind speed, and radiation components to comprehensively assess model performance across different variables and spatial scales.

2.8. Sensible heat flux and advection heat flux

To analyze the three-dimensional structure of heat transport within the urban canopy, we diagnosed both turbulent sensible heat flux and advective heat flux from the LES model output. These diagnostics provide insight into the different mechanisms of heat transfer and their spatial distribution across the study domain.

The 3D resolved turbulent sensible heat flux (H) was calculated from the covariance between vertical velocity (w) and potential temperature (θ) fluctuations:

$$H = \rho c_p \overline{w'\theta'} \quad (\mathrm{W\,m^{-2}}) \tag{4}$$

where ρ is air density (1.2 $\mathrm{kg\,m^{-3}}$), c_p is the specific heat capacity of air at constant pressure (1004 $\mathrm{J\,kg^{-1}\,K^{-1}}$), prime ($'$) indicates the fluctuations calculated as $w' = w - \overline{w}$ and $\theta' = \theta - \overline{\theta}$ with overbar representing the time-averaging over a half-hour interval, and $\overline{w'\theta'}$ represents the vertical turbulent flux of potential temperature. This flux represents the vertical transport of heat by resolved turbulent eddies and was directly output by the PALM4U model at each grid point. Both H and H_{adv} are computed at grid scale only; the subgrid-scale turbulent flux parameterized within PALM4U's 1.5-order closure, together with other residual heat-budget terms, is not included in this diagnostic decomposition.

Advective heat flux quantifies the transport of sensible heat by the time-mean flow and is derived from the advection terms in the thermodynamic energy equation:

$$\left.\frac{\partial\overline{\theta}}{\partial t}\right|_{\mathrm{adv}} = -\overline{u}\frac{\partial\overline{\theta}}{\partial x} - \overline{v}\frac{\partial\overline{\theta}}{\partial y} - \overline{w}\frac{\partial\overline{\theta}}{\partial z} \quad (\mathrm{K\,s^{-1}}) \tag{5}$$

where each advection term combines a wind component ($\mathrm{m\,s^{-1}}$) with a potential temperature gradient ($\mathrm{K\,m^{-1}}$), yielding a local temperature tendency in $\mathrm{K\,s^{-1}}$. This term represents the local rate of temperature change at a fixed point due to the mean wind continuously advecting warmer or cooler air into that location. A negative value indicates that the mean flow brings cooler air (local cooling by advection); a positive value indicates the arrival of warmer air (local warming). The horizontal and vertical advective heat flux components were computed as:

$$H_{\mathrm{adv,h}} = -\rho c_p \left(\overline{u}\frac{\partial\overline{\theta}}{\partial x} + \overline{v}\frac{\partial\overline{\theta}}{\partial y}\right)\Delta z \quad (\mathrm{W\,m^{-2}}) \tag{6}$$

$$H_{\mathrm{adv,v}} = -\rho c_p \left(\overline{w}\frac{\partial\overline{\theta}}{\partial z}\right)\Delta z \quad (\mathrm{W\,m^{-2}}) \tag{7}$$

where $\overline{u}$, $\overline{v}$, and $\overline{w}$ are the time-mean wind components in the x, y, and z directions, respectively, $\frac{\partial\overline{\theta}}{\partial x}$, $\frac{\partial\overline{\theta}}{\partial y}$, and $\frac{\partial\overline{\theta}}{\partial z}$ are the spatial gradients of potential temperature, and $\Delta z = 2\,\mathrm{m}$ is the vertical grid spacing. Multiplying the temperature tendency ($\mathrm{K\,s^{-1}}$) by ρc_p ($\mathrm{J\,m^{-3}\,K^{-1}}$) converts it to a volumetric heating rate ($\mathrm{W\,m^{-3}}$); the subsequent multiplication by Δz (m) then integrates over the layer thickness, yielding a layer-integrated energy flux ($\mathrm{W\,m^{-2}}$) that is directly comparable to the turbulent sensible heat flux H and allows both fluxes to be combined into a single heat budget per model layer. The negative signs follow standard meteorological convention: the flux is positive when heat is transported down the temperature gradient. The total advective heat flux is the sum of both components:

$$H_{\mathrm{adv,total}} = H_{\mathrm{adv,h}} + H_{\mathrm{adv,v}} \tag{8}$$

Spatial gradients of potential temperature were computed using central finite differences with grid spacings of $\Delta x = \Delta y = \Delta z = 2\,\mathrm{m}$. Grid points within buildings (identified by missing values in the model output) and points adjacent to buildings where gradient calculations would be contaminated by boundary effects were masked and excluded from the analysis. These heat flux diagnostics were computed for vertical cross-sections through the urban domain to examine the three-dimensional spatial patterns of turbulent versus advective heat transport mechanisms in relation to urban morphology and surface characteristics, particularly the presence or absence of water bodies.

To isolate the thermal effect of the canal, all diagnostics were computed independently for the CTRL and NOWAT simulations, and scenario differences were formed as:

$$\Delta H = H_{\mathrm{CTRL}} - H_{\mathrm{NOWAT}}, \qquad \Delta\mathrm{Adv} = H_{\mathrm{adv,CTRL}} - H_{\mathrm{adv,NOWAT}} \tag{9}$$

A negative ΔH indicates that the presence of the canal reduces turbulent sensible heat flux relative to the no-water baseline, reflecting a direct surface cooling effect. A negative ΔAdv indicates that the canal enhances the advective import of cool air at that location relative to the baseline, reflecting an advective cooling effect. Conversely, a positive ΔAdv indicates that the canal causes warmer air to be advected toward that location, resulting in a local advective warming effect. The net thermal effect of the canal at each grid point is then the algebraic sum of both contributions:

$$\mathrm{Net\ Effect} = \Delta H + \Delta\mathrm{Adv} \tag{10}$$

It is important to note that the Net Effect is a local quantity: it describes the thermal modification at each individual grid point due to the presence of the canal, not the total heat removed from the urban domain as a whole. Advective cooling at one location is physically the result of cool air being transported away from the canal water surface toward that point; this is necessarily accompanied by compensating advective warming at adjacent locations where the displaced warmer air arrives. Advection therefore primarily redistributes the canal cooling signal spatially across the urban canopy rather than generating additional net cooling at the system level.

Based on the sign of the net effect, each grid point is classified as a net cooling location ($\mathrm{Net\ Effect} < 0$) or a net warming location ($\mathrm{Net\ Effect} \geq 0$). Within each category, the signed advection contribution is computed point-wise as:

$$f_{\mathrm{adv}} = \frac{\Delta\mathrm{Adv}}{|\Delta H| + |\Delta\mathrm{Adv}|} \times 100\% \tag{11}$$

This metric ranges from −100% (advection entirely responsible for local cooling) to +100% (advection entirely responsible for local warming), and preserves the thermal direction of the advective contribution while normalizing by total local effect magnitude. Spatial distributions of f_{adv} are examined separately for net cooling and net warming regions within vertical cross-sections through the canal-influenced urban canopy layer, allowing the relative roles of turbulent and advective mechanisms to be quantified and compared between the two wind-canal orientations.

3. Evaluations

3.1. Mesoscale meteorology

The WRF simulation successfully captures the synoptic meteorological conditions during the study period. Evaluation against KNMI Schiphol observations shows excellent performance for temperature and shortwave radiation (R^2 = 0.92 and 0.98, RMSE = 1.2°C and 43 W $\mathrm{m^{-2}}$, respectively), Fig. S4. These performance metrics are consistent with typical WRF skill reported in previous urban meteorological studies, where temperature and radiation are generally well-captured while humidity and wind speed show larger uncertainties due to their sensitivity to local surface characteristics and subgrid-scale processes (Koopmans et al., 2023; Ronda et al., 2017). The simulation accurately reproduces the temporal evolution of key meteorological variables, including diurnal temperature variations (15 to 31°C), solar radiation patterns (peak ~800 W $\mathrm{m^{-2}}$), and light wind conditions (0 to 6 m $\mathrm{s^{-1}}$). This demonstrates that WRF provides reliable mesoscale forcing for the nested LES.

3.2. Near-surface meteorology

The urban near-surface meteorology evaluation is presented in Fig. 2, with quantitative statistics (RMSE and IoA) displayed directly in each subplot. LES explicitly resolves the urban canyon geometry and provides meteorological variables at the actual measurement heights (approximately 4 m) within the street canyons where the AAMS stations are located. The evaluation focuses on the period after the 3-hour model spin-up to ensure statistical robustness.

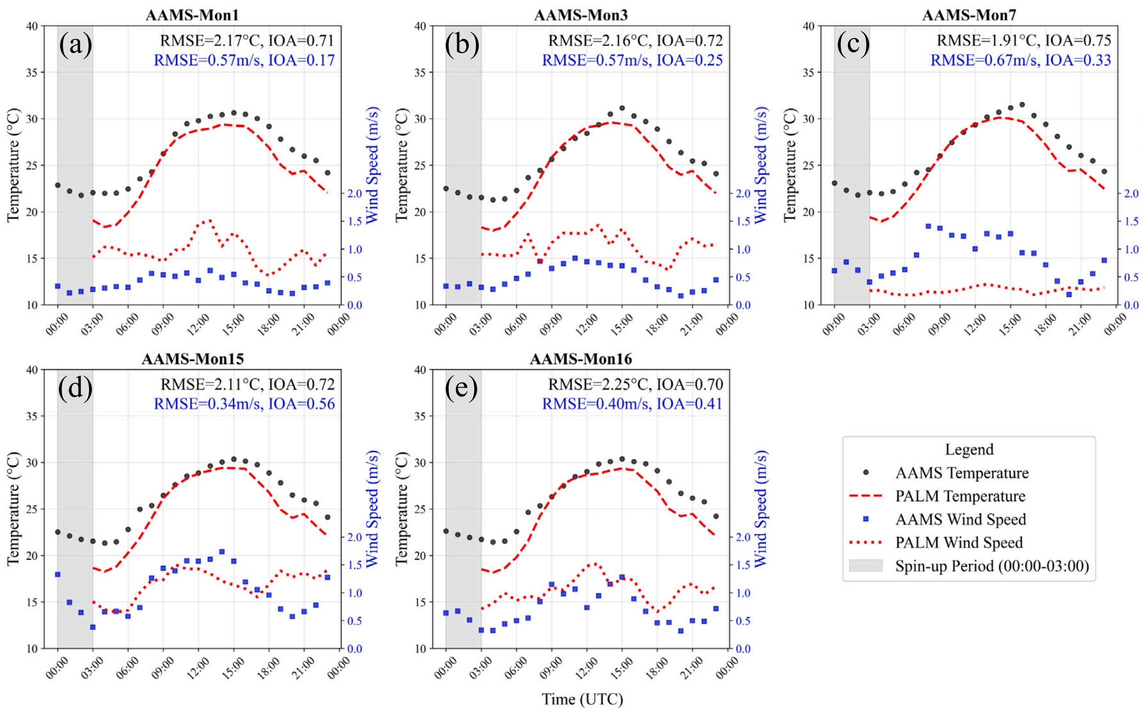

Fig. 2. Near-surface temperature (left y-axis) and wind speed (right y-axis) on 13 Aug, 2022 at five AAMS stations. Observations shown as black dots (temperature) and blue squares (wind speed); PALM4U LES 4-m output shown as red dashed line (temperature) and red dotted line (wind speed). RMSE and IoA statistics displayed in each subplot (black text for temperature, blue text for wind speed). The gray shaded area (00:00–03:00 UTC) indicates the model spin-up period excluded from statistical analysis.

For temperature (black lines and text in Fig. 2), LES captures the diurnal cycle well across all five AAMS stations, with temperatures ranging from approximately 18°C during nighttime to 30°C during peak afternoon hours. The model achieves a mean RMSE of 2.1°C and IoA of 0.72 across all stations, demonstrating good agreement with observations. These results are comparable to the PALM4U validation study by Resler et al. (2017), which reported an RMSE of 2.0°C for near-surface air temperature during summer daytime simulation. Individual station statistics show RMSE values ranging from 1.8 to 2.5°C and IoA from 0.68 to 0.75, with the variability reflecting differences in local urban morphology (building height, street canyon aspect ratio, and surface materials). The model exhibits slight underestimation during the warmest afternoon periods at some stations.

Wind speed evaluation (square dots and text in Fig. 2) demonstrates PALM4U's capability to represent the sheltering effects of buildings and the reduced wind speeds within urban canyons. The observed wind speeds at the canyon-level stations remain consistently low (<2 m s^{-1}) due to building sheltering effects. PALM4U model successfully captures this low-wind-speed environment through its building-resolving framework, achieving a mean RMSE of 0.50 m s^{-1} and IoA of 0.40 across all stations, comparable to the RMSE of 1.0 m s^{-1} reported by Resler et al. (2017). The moderate IoA reflects the challenge of predicting highly variable canyon winds influenced by local turbulence, exact building configuration, and thermal effects. Nevertheless, the evaluation shows that LES reproduces the canyon-level wind field with reasonable accuracy and is therefore suitable for investigating urban heat transport processes in this study.

3.3. Radiative and turbulent fluxes

Radiative and turbulent flux evaluation focuses on net radiation and sensible heat flux measured by the combined EC system and net-radiometer (Fig. 3). Net radiation observations were recorded at 1-minute intervals and averaged to 30-minute periods to match the model output frequency; confidence intervals represent the standard deviation within each averaging period. Net radiation (Fig. 3b) shows excellent agreement, with RMSE of 12.9 W m^{-2} and IoA of 1.00. The model accurately reproduces the diurnal cycle, with values reaching approximately 600 W m^{-2} at midday and approaching zero during nighttime hours. This near-perfect performance indicates that the radiative transfer scheme and surface albedo representation are well captured in the model.

Sensible heat flux (Fig. 3a) shows an excellent overall agreement (IoA = 0.94) with an RMSE of 46.5 Wm^{-2} and negative bias of −16.4 W m^{-2}. This bias falls within the typical measurement uncertainty of EC systems (approximately 10% for sensible heat flux Järvi et al., 2018; Nordbo et al., 2012), which corresponds to ±20 W m^{-2} at peak flux conditions. Despite the bias, the model successfully captures the temporal evolution and diurnal pattern of turbulent heat exchange between the urban surface and atmosphere. Turbulent heat flux evaluation remains rare in urban LES studies due to the scarcity of direct EC measurements in complex urban environments (Lieber et al., 2025; Resler et al., 2017); the strong agreement demonstrated here provides robust evidence that PALM4U model adequately represents surface-atmosphere energy coupling, which is essential for reliable quantification of sensible heat reduction and canal-induced heat transport in this study.

4. Thermal conditions and flow patterns

4.1. General patterns

The diurnal cycle of 2-m air temperature reveals distinct thermal characteristics between pavement and water surfaces (Fig. 4a). Throughout the day, air temperature above pavement ranges from 18.1°C to 29.3°C, while air temperature above water ranges from 18.0°C to 28.8°C. Air above both surfaces exhibit similar nocturnal temperatures around 18.0°C, followed by a steady warming period from sunrise until peak temperatures are reached around midday (12:00 to 15:00 UTC). Air above water surface maintains consistently lower air temperatures during the daytime heating phase, with the

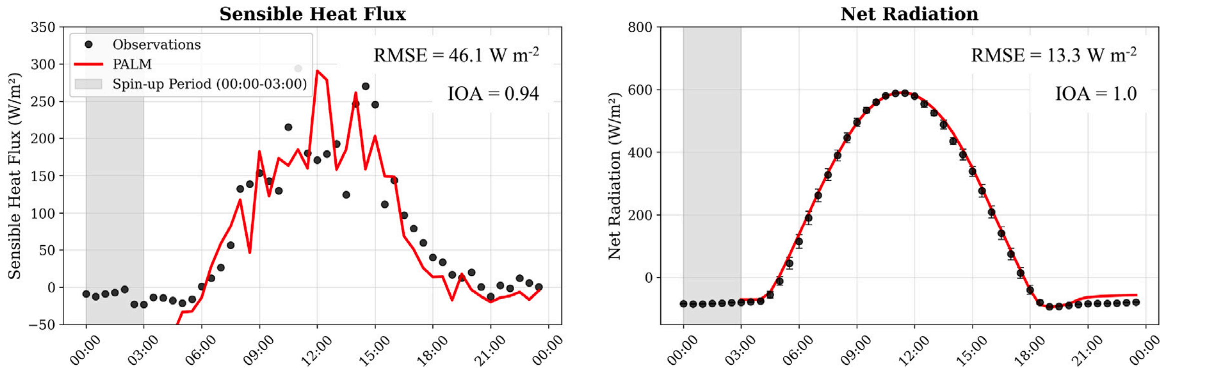

Fig. 3. PALM4U-simulated (red line) versus observed (black dots) surface energy fluxes at the M007 eddy covariance tower on 13 Aug, 2022: (a) sensible heat flux, (b) net radiation. RMSE and IoA statistics are displayed in each subplot. The gray shaded area (00:00–03:00 UTC) indicates the model spin-up period excluded from statistical analysis. Net radiation observations are shown with confidence intervals representing the standard deviation of 1-minute measurements within each 30-minute averaging period.

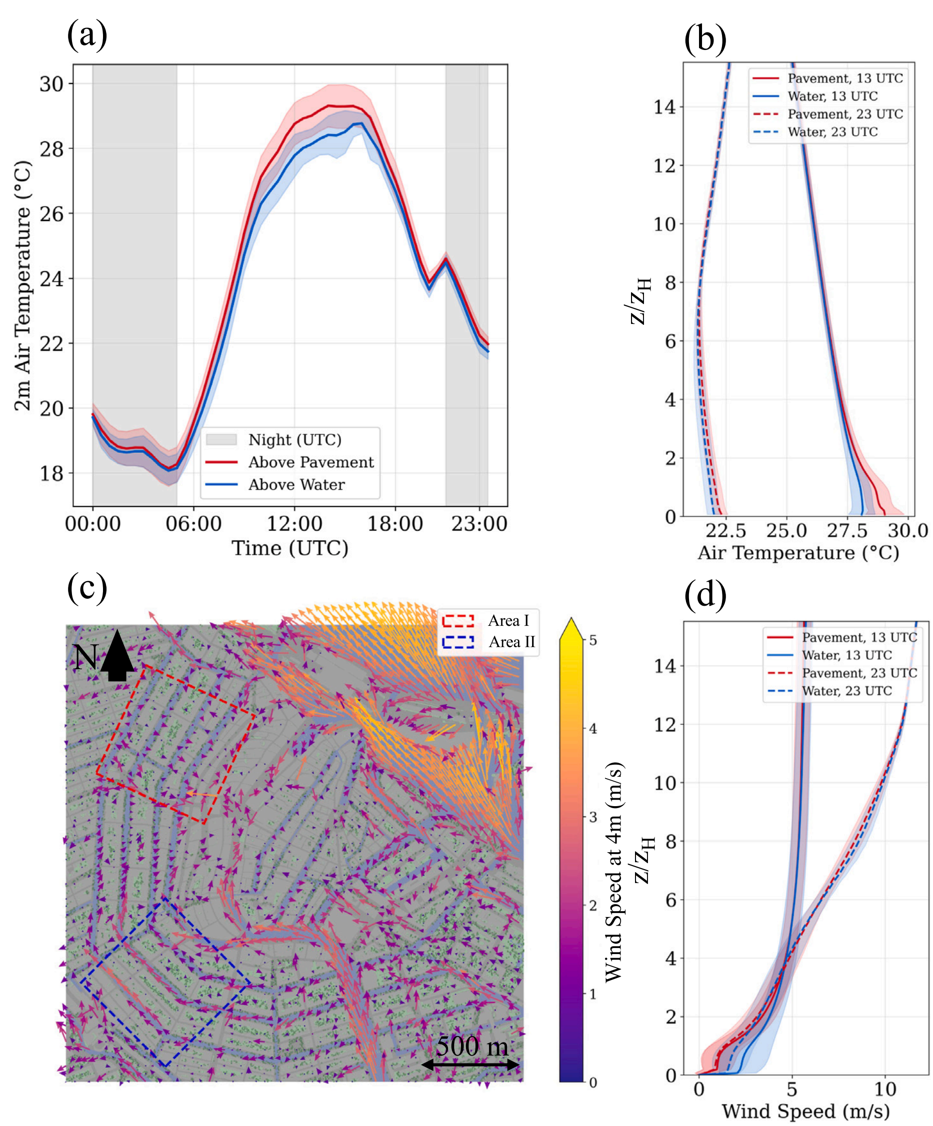

Fig. 4. Thermal and flow characteristics from the PALM4U LES CTRL case: (a) diurnal cycle of 2-m air temperature above pavement (red) and water (blue) surfaces, with shaded areas indicating standard deviation and gray shading denoting nighttime periods (UTC); (b) vertical profiles of spatially averaged air temperature at 13:00 UTC (solid lines) and 23:00 UTC (dashed lines) above pavement (red) and water (blue); (c) spatial distribution of near-surface wind speed at 4 m height at 13:00 UTC, with wind vectors overlaid and two selected areas (Area I in red dashed box with wind perpendicular to canals, Area II in blue dashed box with wind parallel to canals) marked for detailed analysis; (d) vertical profiles of spatially averaged horizontal wind speed at 13:00 UTC (solid lines) and 23:00 UTC (dashed lines) above pavement (red) and water (blue).

Table 3
Geometric and surface characteristics of Area I and Area II.

Metric	Area I	Area II
Mean building height (m)	15.7	15.0
Building coverage (%)	40.9	44.2
Water coverage (%)	18.1	16.3
Tree coverage (%)	11.0	12.6
Mean canal width (m)	25.1	23.6
Mean canyon width (m)	43.5	41.5
Wind-canal angle (°)	87.6	3.0

maximum temperature difference of approximately 0.5°C occurring during peak heating hours. After 18:00 UTC, air over both surfaces shows rapid cooling, with temperatures converging during the evening transition period. The vertical profiles of air temperature (Fig. 4b) further illustrate these thermal differences at two contrasting times: 13:00 UTC (daytime) and 23:00 UTC (nighttime). At 13:00 UTC and $z/z_H = 1$, air temperature above pavement reaches 28.6°C, while above water it is 28.0°C, representing a difference of 0.60°C near the surface. This temperature difference diminishes with height, with the profiles converging at approximately $z/z_H = 4$. During nighttime (23:00 UTC), the thermal contrast nearly disappears, with temperatures of 22.1°C above pavement and 21.9°C above water at $z/z_H = 1$, a difference of only 0.2°C.

The spatial distribution of near-surface wind at 13:00 UTC (Fig. 4c) reveals complex flow patterns influenced by the urban morphology and water bodies within the domain. The highest wind speeds occur over the large water patch in the top-right portion of the domain, where the absence of surface roughness elements allows for stronger, more uniform flow. The vertical profiles of horizontal wind speed (Fig. 4d) demonstrate the development of the boundary layer. At 13:00 UTC and $z/z_H = 1$, wind speed above water surfaces is higher than above pavement, a difference of 1.2 m s^{-1} attributable to the lower surface roughness over water. Wind speeds increase steadily with height for both surface types, reaching approximately 5.8 m s^{-1} at the top of the domain, and the profiles converge above $z/z_H = 3.8$. During nighttime (23:00 UTC), the water-pavement contrast persists but is reduced, with wind speeds of 2.0 m s^{-1} above water and 1.3 m s^{-1} above pavement at $z/z_H = 1$.

4.2. Contrasting wind-canal configurations

Based on relative wind directions, two representative areas are selected for detailed analysis (Fig. 4c): Area I (red), where the wind direction is approximately perpendicular to the canals, and Area II (blue), where the wind direction is nearly parallel to the canals. To confirm that the two areas are comparable in terms of urban morphology and surface composition, and that wind-canal orientation is the primary distinguishing factor, a systematic geometric and surface characterization was conducted (Table 3). The dominant wind direction was diagnosed at 15 m height (near rooftop level), yielding a wind-canal angle of 87.6° in Area I and 3.0° in Area II, confirming the near-perpendicular and near-parallel orientations, respectively. The two areas exhibit closely comparable urban morphology. These contrasting wind-canal orientations are examined in subsequent analysis to assess their impact on cooling effectiveness, turbulent heat flux exchange, and thermal advection mechanisms.

The spatial distributions of 2-m air temperature at 13:00 UTC over the two selected areas show similar mean values but distinct spatial patterns (Fig. 5). Area I exhibits a temperature mean of 28.9°C (Fig. 5a), and Area II shows a mean of 28.8°C (Fig. 5c). Despite similar means, the two areas display different thermal variability. In Area II, cooler temperatures (bluish colors) are visible over the canal surfaces, while Area I shows relatively warmer near-surface air over the water bodies. Additionally, the two street canyons on the right side of Area I that lack water features exhibit markedly higher temperatures (intense red color) than adjacent canyons containing canals.

Fig. 5b,d show vertical cross-sections of flow structures in each area. In Area I, the projected wind vectors show an anticlockwise circulation pattern within the street canyon, with right-to-left flow over and near building height and left-to-right flow near the street surface, reflecting the mechanical interaction between the perpendicular prevailing wind and the canyon geometry. In Area II, the vertical slice displays predominantly vertical wind vectors, indicating a thermally driven circulation: air descends over the water surface and ascends over pavement and building surfaces. The predominantly vertical motion in this cross-section occurs because the prevailing wind is parallel to the canal axis and thus perpendicular to the slice orientation, allowing the thermal circulation to be clearly visible while the along-canyon flow component is not captured in this view. To further quantify these circulation patterns, the cross-slice vorticity is calculated for a zoomed region spanning $z/z_H = 0$ to 3 vertically (Fig. 6). In Area I, positive vorticity values (red colors, indicating counterclockwise rotation) (Fig. 6a), confirming the shear-driven anticlockwise circulation pattern within the canyon. Locations with wide street canyon (30 to 130 m along the slice) exhibit less negative vorticity compared to the narrow canyons, which show larger negative values. These recirculating vortices locally reverse the wind direction thereby transporting the lower temperature air over the canals toward the streets. This mechanism will be further elaborated in the upcoming sections.

In contrast, in Area II, slightly positive vorticity values (light blue color, indicating slight clockwise rotation) are present over the street canyons around 300 m and 590 m (Fig. 6b). The figure shows that the strength of the recirculating vortices is lower compared to Area I. These contrasting vorticity patterns highlight the difference in flow dynamics between the two wind-canal orientations.

To assess the robustness of the simulated circulation patterns with respect to the prescribed water temperature, two additional sensitivity simulations were performed with canal water temperatures of 294 K and 296 K, 1 K relative to the baseline. The domain-mean cross-sectional vorticity in Area I amounts to 0.105 s^{-1} (294 K), 0.088 s^{-1} (295 K), and 0.092 s^{-1} (296 K), with an average grid-point sensitivity of approximately 0.010 s^{-1} K^{-1}. In Area II, the corresponding values are near-zero across all three cases. Fig. S5 confirms that the counterclockwise recirculation pattern in Area I and the weaker clockwise rotation in Area II are qualitatively preserved across all three scenarios. These results indicate that the prescribed water temperature does not substantially alter the wind field or canyon circulation, and that the mechanistic conclusions drawn from the baseline simulation are robust to a 1 K uncertainty in water temperature.

The simulated flow structures are consistent with well-established urban canyon flow regimes documented in wind tunnel experiments and numerical studies. In Area I, where the wind is near-perpendicular to the canyon axis, the single recirculating vortex with reversed near-surface flow is characteristic of the skimming flow regime, commonly observed in canyons with aspect ratios (H/W) approaching or exceeding unity (Letzel et al., 2008; Oke, 1988; Soulhac et al., 2011). The shear-driven anticlockwise circulation and the dependence of vortex intensity on canyon width are also consistent with findings from previous LES studies of urban street canyons (Letzel et al., 2008). In Area II, the weaker vorticity and predominantly thermally driven vertical circulation under near-parallel wind conditions are likewise in agreement with the reduced mechanical mixing expected when the along-canyon wind component dominates (Soulhac et al., 2011). This qualitative agreement with canonical canyon flow behavior provides confidence in the physical realism of the simulated circulation structures, even in the absence of direct field measurements of canyon-scale flow at the study site.

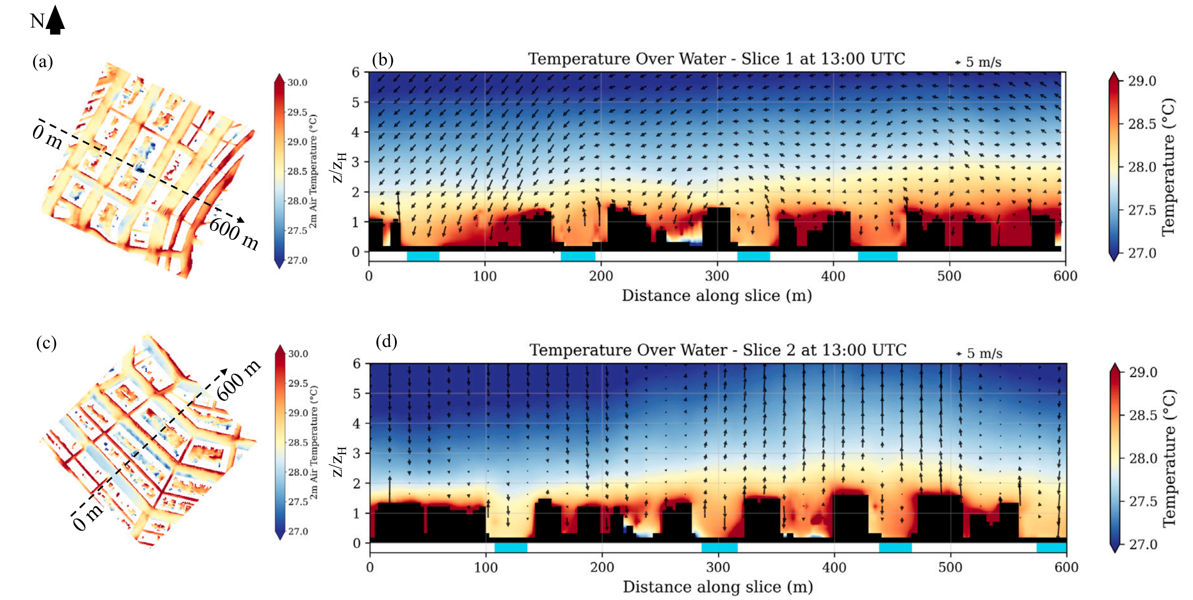

Fig. 5. Thermal and flow characteristics at 13:00 UTC for the two selected areas: (a) 2-m air temperature spatial distribution over Area I with dashed arrow indicating the cross-section cutting direction; (b) vertical cross-section along the cutting line in Area I showing air temperature field (color contours) and projected wind vectors; (c) 2-m air temperature spatial distribution over Area II with dashed arrow indicating the cross-section cutting direction; (d) vertical cross-section along the cutting line in Area II showing air temperature field (color contours) and projected wind vectors. Black structures represent buildings, cyan areas represent water surfaces.

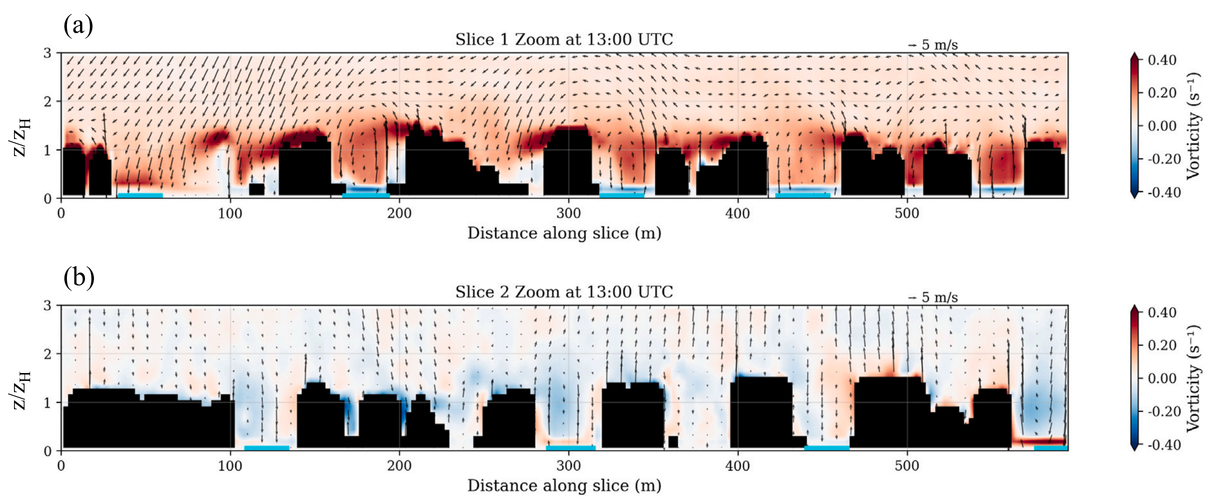

Fig. 6. Vertical cross-sections showing vorticity fields (contour shading) and projected wind vectors at 13:00 UTC for (a) Area I (wind perpendicular to canal) and (b) Area II (wind parallel to canal). Negative vorticity values (blue) indicate counterclockwise rotation, while positive values (red-orange) indicate clockwise rotation. Black structures represent buildings, cyan areas represent water surfaces.

5. Canal impact on urban heat exchange

5.1. Temperature difference

To quantify the cooling effect of canal water surfaces on the urban environment, we compare air temperature between the CTRL case and the NOWAT case. The diurnal evolution of 2-m air temperature difference over pavements shows minimal differences during nighttime (before 06:00 UTC and after 18:00 UTC) for both areas, with values near zero (Fig. 7a). As solar heating intensifies after sunrise, the cooling effect strengthens progressively, reaching peak values around 13:00 to 14:00 UTC. This indicates that canal water surfaces reduce near-surface air temperature over adjacent land areas by up to 0.7°C during peak heating hours. Vertically, this cooling effect is most pronounced near the surface and diminishes with height (Fig. 7b). At 13:00 UTC, the maximum average cooling of approximately −0.5°C occurs at the near surface, decreasing to about −0.3°C at $z/z_H = 1$, and nearly vanishing above $z/z_H = 4$. During nighttime (23:00 UTC), the vertical temperature difference becomes negligible throughout the boundary layer, consistent with reduced thermal contrast between water and pavement surfaces after sunset. While these values represent the mean cooling effect, large variability in the values indicates spatial heterogeneity in the cooling effect, which will be explained next. Sensitivity simulations with water temperatures of 294 K and 296 K indicate that a 1 K perturbation shifts the mean near-surface cooling by approximately 0.04 Kelvin per Kelvin in Area I and 0.03 Kelvin per Kelvin in Area II on average, confirming that the qualitative cooling signal and its spatial structure are robust to this uncertainty (Figures S6a and S6b).

The 2-m air temperature difference maps at 13:00 UTC reveal distinct spatial heterogeneity in cooling between the two areas (Fig. 8). In

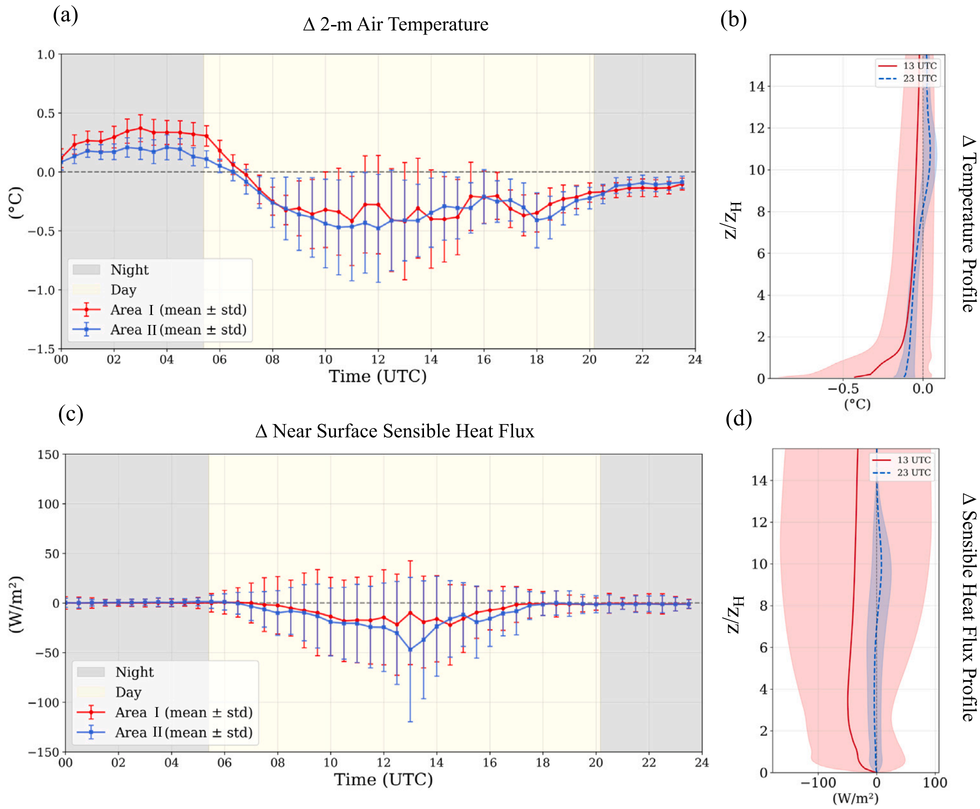

Fig. 7. Diurnal cycle and vertical profiles of temperature and sensible heat flux differences (CTRL–NOWAT): (a) diurnal cycle of Δ 2-m air temperature over land areas in Area I (red) and Area II (blue), with error bars indicating standard deviation and gray shading denoting nighttime periods (UTC); (b) vertical profiles of Δ air temperature over all land grids in the domain at 13:00 UTC (solid lines) and 23:00 UTC (dashed lines), with shaded areas showing standard deviation; (c) diurnal cycle of Δ near-surface sensible heat flux over land areas in Area I (red) and Area II (blue); (d) vertical profiles of Δ sensible heat flux at 13:00 UTC (solid lines) and 23:00 UTC (dashed lines), with shaded areas showing standard deviation. Negative values indicate cooling or reduced heat flux in the CTRL case relative to NOWAT.

Area I, the cooling pattern is highly asymmetric within street canyons (Fig. 8a). The most intense cooling, reaching up to −1.5°C, concentrates on the right side of narrow street canyons containing canals, while the opposite side experiences only modest cooling of approximately −0.2°C to −0.5°C. Conversely, Area II displays a more uniform cooling distribution of around −0.7°C that spreads evenly across the entire width of canal-containing street canyons (Fig. 8c). These area-averaged cooling magnitudes are broadly consistent with the 0.2 to 0.6°C afternoon air temperature reductions reported by Jacobs et al. (2020) for typical Dutch urban water bodies, while the strong within-canyon spatial heterogeneity highlights that local building configuration and wind direction relevant to canal orientation critically determine where thermal benefits are realized.

Vertical cross-sections reveal the three-dimensional structure of canal-induced cooling and its interaction with street canyon flow dynamics (Fig. 9). In Area I, cooling is predominantly confined below $z/z_H = 2$, with slight cooling extending to $z/z_H = 3$ (Fig. 9a). Within narrow canyons with canals, cooling is strongly concentrated on the right side, reaching more than −1.0°C, demonstrating the asymmetric cooling pattern. As the background wind flows from right to left over rooftops, canyon circulation transports cool air preferentially to the right side. Due to weaker circulation in the wider geometry (Fig. 6), the wide street canyon at 30 to 130 m along the slice lacks this pronounced asymmetry. Cooling also extends beyond canyons containing water features. The street canyon without a canal at 250 to 300 m still experiences cooling through horizontal advection from the adjacent canal-cooled canyon. Some streets lacking canals show minor near-surface warming (light yellow), with the warming signal limited to approximately 0.1°C. In Area II (Fig. 9b), cooling is more vertically uniform within each canal-containing canyon and confined primarily to those canyons, with minimal lateral spreading to adjacent street canyons. This containment reflects the different flow regime when wind is parallel to the canal axis, where along-canal flow restricts cross-canyon transport.

5.2. Sensible heat flux difference

Canal water surfaces substantially alter sensible heat flux exchange between the surface and atmosphere. The diurnal cycle of near-surface sensible heat flux difference shows considerable spatial variability, evidenced by large standard deviations (Fig. 7c). At night, median values remain near zero in both areas. The median values reach negative peaks around 13:00 to 14:00 UTC of approximately −20 W m^{-2} to −40 W m^{-2}. However, the boxes extend over a substantial range, spanning from approximately −100 W m^{-2} to +20 W m^{-2}. This large variability reflects the heterogeneous nature of the domain, which includes land grids both adjacent to and distant from canal surfaces. The vertical profile (Fig. 7d) shows how this turbulent heat flux difference extends vertically through the boundary layer, with the mean difference approximately −50 W m^{-2} at $z/z_H = 2$ at 13:00 UTC. Standard deviation shading is also substantially wider than that observed for temperature profiles, extending over 50 W m^{-2}. This large standard deviation arises from including all pavement in the domain, encompassing both areas strongly influenced by nearby canals and areas where canal effects are minimal or absent. During nighttime (23:00 UTC), both median

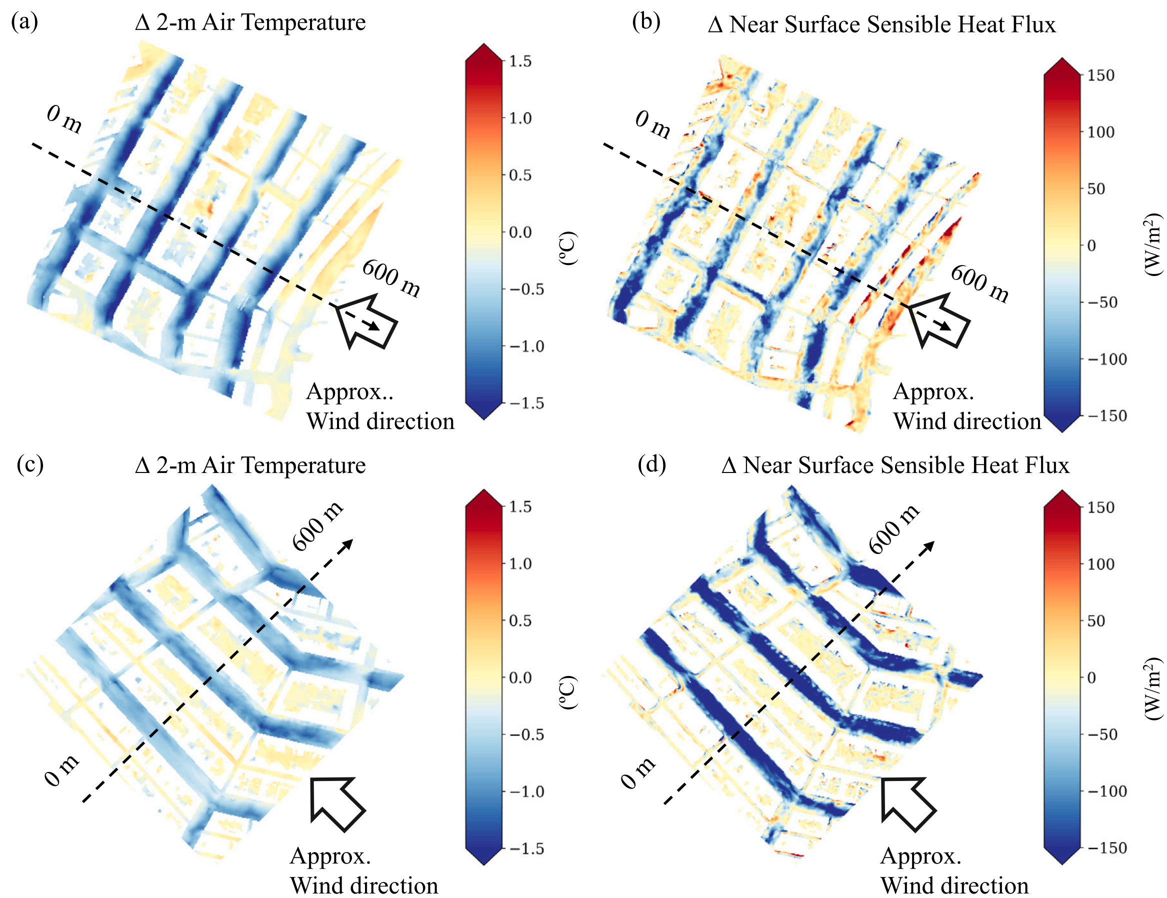

Fig. 8. Spatial distributions of temperature and sensible heat flux differences (CTRL − NOWAT) at 13:00 UTC: (a) Δ 2-m air temperature over Area I; (b) Δ near-surface sensible heat flux over Area I; (c) Δ 2-m air temperature over Area II; (d) Δ near-surface sensible heat flux over Area II. Dashed arrows indicate the cross-section cutting directions used in subsequent vertical slice analysis. The dominant wind direction above the canopy, as shown by the large outlined arrow, is approximately perpendicular to the canals in Area I, and approximately parallel to the canals in Area II. Negative temperature values (blue) indicate a cooling effect, while negative heat flux values (blue) indicate reduced upward sensible heat flux in the CTRL case compared to NOWAT.

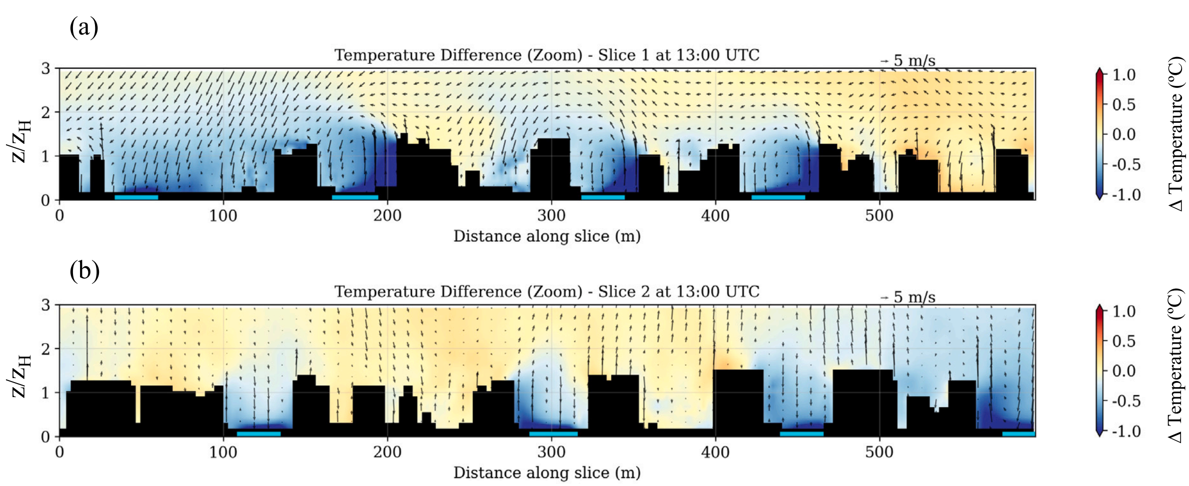

Fig. 9. Vertical cross-sections of temperature difference (CTRL − NOWAT) at 13:00 UTC: (a) Δ air temperature field (color contours) and projected wind vectors for Area I (wind perpendicular to canal); (b) Δ air temperature field (color contours) and projected wind vectors for Area II (wind parallel to canal). Black structures represent buildings, cyan areas represent water surfaces. The vertical extent is zoomed to z/z_H = 0 to 3 to emphasize near-surface cooling patterns.

difference and standard deviation become negligible. Sensitivity tests with water temperature perturbations show that the mean sensible heat flux difference changes by less than 0.4 W m^{-2} per Kelvin in both areas (Area I: 0.29 W m^{-2}; Area II: 0.33 W m^{-2} per Kelvin), which is small relative to the peak median differences of −20 to −40 W m^{-2}, suggesting the conclusions are not materially sensitive to the prescribed water temperature (Figures S6c and S6d).

Spatial distributions of near-surface sensible heat flux difference at 13:00 UTC follow patterns similar to temperature difference but with greater spatial heterogeneity and more pronounced small-scale

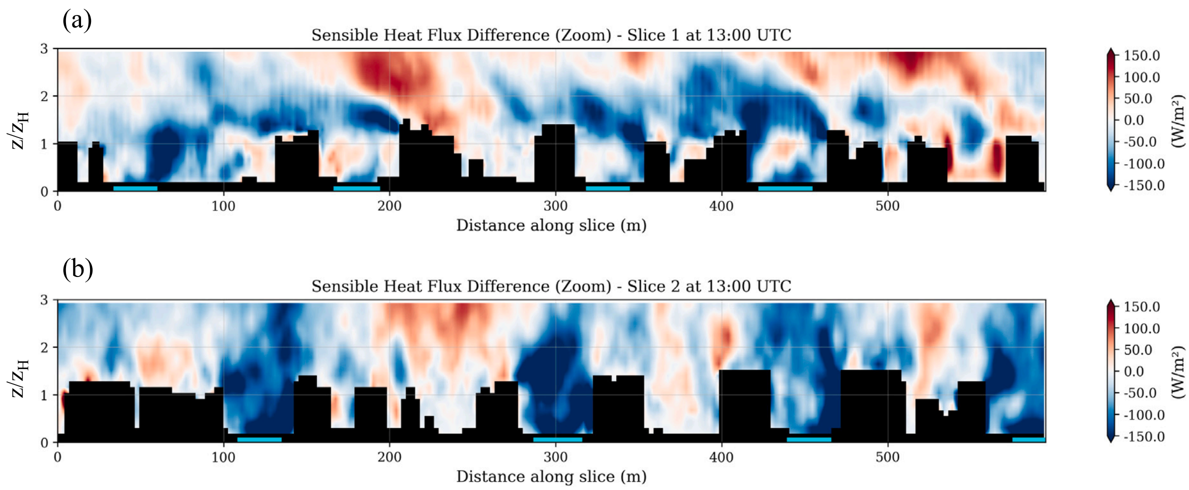

Fig. 10. Vertical cross-sections of sensible heat flux difference (CTRL – NOWAT) at 13:00 UTC: (a) Δ sensible heat flux field for Area I (wind perpendicular to canal); (b) Δ sensible heat flux field for Area II (wind parallel to canal). Black structures represent buildings, cyan areas represent water surfaces. The vertical extent is zoomed to z/z_H = 0 to 3. Negative values (blue) indicate reduced upward sensible heat flux in the CTRL case compared to NOWAT, while positive values (red) indicate enhanced upward sensible heat flux.

variability (Fig. 8b,d). In Area I, strong negative values reaching −150 W m^{-2} concentrate over and immediately adjacent to canal surfaces, with the most intense reductions occurring on one side of street canyons (Fig. 8b). Positive values, indicating locally increased sensible heat flux in the CTRL case, appear in scattered patches throughout the domain, creating a fragmented spatial pattern. In Area II, the sensible heat flux difference displays a more organized structure, with negative values of approximately −100 W m^{-2} to −150 W m^{-2} concentrated primarily over canal surfaces and their immediate vicinity (Fig. 8d).

Fig. 10 provides further detailed insight into the cross-section structure of sensible heat flux modification. In Area I, the pattern exhibits considerable vertical and horizontal complexity (Fig. 10a). Over water surfaces, strong negative values are present near the surface, indicating reduced upward sensible heat flux in the CTRL case. At the mid-canyon level, z/z_H = 0.5 above water surfaces, localized positive values appear, suggesting enhanced upward heat flux in these regions. Negative values form plume-like structures that extend upward from z/z_H = 1 to 2, following the canyon circulation pattern. These structures are particularly visible in narrow canyons where the right side shows coherent negative plumes extending vertically. In Area II, negative values extend vertically from the surface up to z/z_H = 3 above canal surfaces, forming more vertically elongated structures (Fig. 10b). Unlike Area I, there is no consistent layer of altered sensible heat flux between z/z_H = 1 and z/z_H = 2, spanning across the domain. Instead, sensible heat flux modifications are confined primarily to vertical columns above canals, with minimal horizontal spreading to adjacent street canyons. This vertical confinement is consistent with temperature difference patterns observed in Area II, reinforcing the influence of wind direction relative to canal orientation on the spatial distribution of thermal effects.

5.3. *Water-induced thermal advection*

To further understand the mechanisms by which canal water surfaces affect urban thermal conditions, we examine the difference in microscale thermal advection between the CTRL and NOWAT cases. Thermal advection represents the transport of heat by mean flow motion or persistent flow structures. The difference in total advection (horizontal plus vertical components) between CTRL and NOWAT reveals how the presence of water modifies heat transport patterns. Positive values indicate advective warming induced by water presence, while negative values indicate advective cooling.

Vertical cross-sections of advection difference reveal distinct spatial patterns in the two areas (Fig. 11). In Area I, positive values (red) appear directly above water surfaces, indicating that water presence induces local advective warming at these locations (Fig. 11a). Strong negative values (dark blue) concentrate on the right side of canals where the canyon vortex drives downward flow (Fig. 6a), while positive values (red) appear on the left side pavement where upward flow occurs. This spatial pattern directly reflects the anticlockwise vortex circulation. A coherent negative plume extends from z/z_H = 1 to 1.5 on the right side of narrow canyons, following the circulation pattern and indicating sustained advective cooling in this region. The magnitude of advection difference is generally smaller than the sensible heat flux difference, with maximum values reaching approximately 50 W m^{-2} compared to sensible heat flux differences exceeding 100 W m^{-2}. This indicates that the water surface is warmed by the horizontal heat transport while the adjacent pavements are cooled due to this thermal advection.

In Area II (Fig. 11b), positive values also appear directly above water surfaces, but moderate negative values are present on both sides of the pavement adjacent to canals, rather than being concentrated on one side as in Area I. There is no pronounced negative plume structure near or above building roof level, in contrast to Area I. The advective modifications remain more vertically confined above the canals without the horizontal asymmetry observed in Area I. These contrasting advection patterns between Area I and Area II corroborate the finding of Chen et al. (2026) that horizontal advection is the dominant cooling mechanism in urban blue spaces, while further demonstrating that the effectiveness of advective heat redistribution depends critically on wind-canal orientation and the resulting canyon flow structure.

6. Discussions

6.1. *Relative contribution of advection to total thermal effects*

To further quantify the relative importance of sensible heat flux reduction versus heat advective mechanisms in producing the observed thermal modifications, we analyze the signed contribution of advection to the total thermal effect. The net thermal effect is calculated as the algebraic sum of the sensible heat flux difference (ΔH) and the advection difference (ΔAdv) between CTRL and NOWAT scenarios: $\text{Net Effect} = \Delta H + \Delta Adv$. We classify each location into two categories based on the sign of this net effect: net warming regions ($\text{Net Effect} \geq 0$) and net cooling regions ($\text{Net Effect} < 0$). Within each category, we calculate the signed advection contribution as: $\text{Advection Contribution (\%)} = \frac{\Delta Adv}{|\Delta H|+|\Delta Adv|} \times 100$, ranging from −100% (pure advective cooling) to

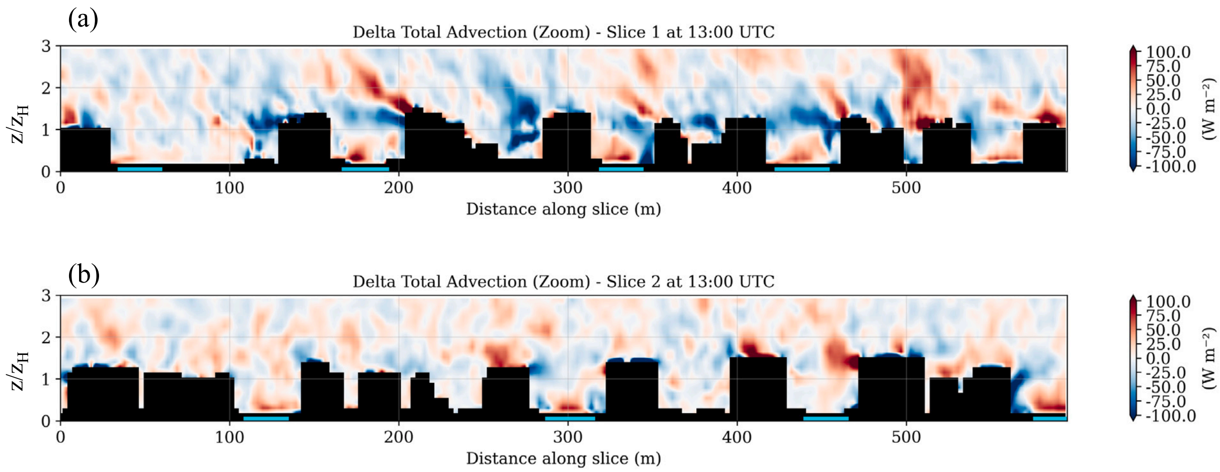

Fig. 11. Vertical cross-sections of total advection difference (CTRL – NOWAT) at 13:00 UTC: (a) Δ total advection heat flux field (color contours) for Area I (wind perpendicular to canal); (b) Δ total advection heat flux field (color contours) for Area II (wind parallel to canal). Black structures represent buildings, cyan areas represent water surfaces. The vertical extent is limited to $z/z_H = 0$ to 3. Positive values (red) indicate advective warming induced by water presence, while negative values (blue) indicate advective cooling.

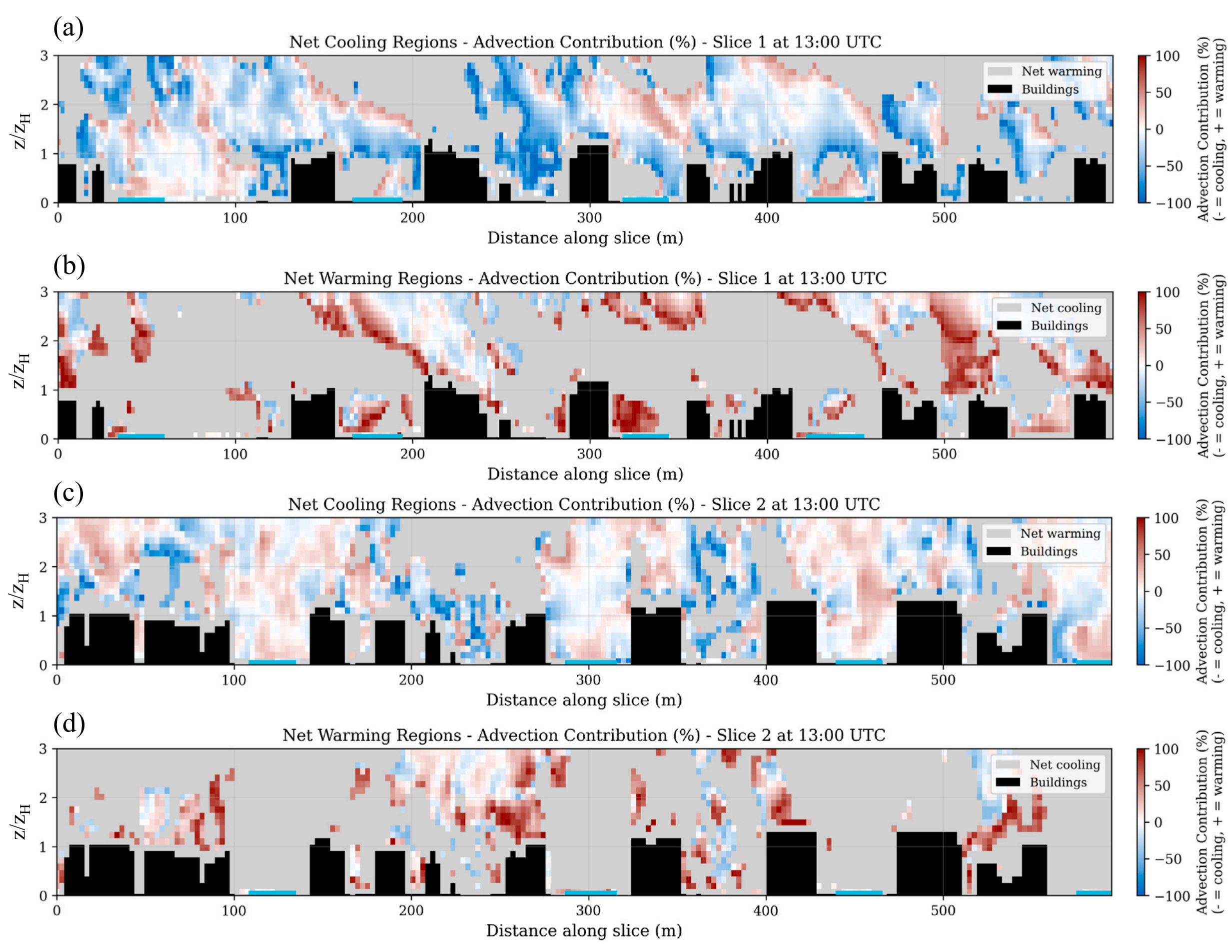

Fig. 12. Vertical cross-sections showing advection contribution to total thermal effects at 13:00 UTC for Area I (wind perpendicular to canal, panels a-b) and Area II (wind parallel to canal, panels c-d): (a) net cooling regions in Area I; (b) net warming regions in Area I; (c) net cooling regions in Area II; (d) net warming regions in Area II. In each panel, the colorbar represents advection contribution from −100% (pure advective cooling) to +100% (pure advective warming). Light gray areas indicate regions with opposite net effect (masked for clarity). Black structures represent buildings, cyan markers represent water surfaces. The vertical extent is limited to $z/z_H = 0$ to 3.

+100% (pure advective warming). This metric preserves the thermal direction of advection while quantifying its relative magnitude.

The spatial distribution reveals contrasting advective mechanisms between the two wind-canal orientations (Fig. 12). In Area I's net cooling regions (Fig. 12a), strong advective cooling (−60%) dominates over pavement on the right side of canals below canopy level ($z/z_H \leq 1$), where upward flows within the canyon vortex effectively redistribute cool air from the water surface. At and above rooftop level ($z/z_H \geq 1$), coherent cooling plumes extend from canal-containing canyons (up to −80%), propagating downwind. In net warming regions (Fig. 12b), advection warming (+40 to +80%) dominates on the left side of water surfaces, where downward and left-to-right flows driven by the canyon vortex transport warmer air from above and from the heated pavement, thereby enhancing net warming. Above canopy level, net warming zones originate at the building edges and expand progressively downwind across the rooftops. Overall, the canyon vortex redistributes cool air from the water surface to surrounding areas, such that advection accounts for the dominant share of cooling over adjacent pavement and above the canopy, extending the spatial footprint of the water surface cooling effect. It should be noted that the advective cooling in net-cooling regions and the advective warming in net-warming regions are physically complementary, together representing a spatial redistribution of the canal-cooling signal rather than a net increase in heat removal from the urban system. At the pedestrian levels ($z/z_H \leq 0.5$), this advective redistribution is the primary mechanism determining the spatial extent of canal-induced air temperature reduction beyond the water surface itself, and is strongly controlled by wind-canal orientation. Sensitivity simulations with water temperature perturbations show that the advection contribution shifts by approximately 10.6% in net cooling regions and 7.6% points in net warming regions per Kelvin, indicating that while the absolute magnitudes are moderately sensitive to the prescribed water temperature, the dominant role of advection and the overall spatial structure remain consistent across all three cases (Figure S8).

In Area II's net cooling regions (Fig. 12c), warming advection (+10 to +40%) extends vertically over water surfaces, reflecting that warmer air from surrounding surfaces is transported toward the water surface. Weak advection cooling (−20 to −40%) appears over adjacent pavement on both sides of the canal. The net cooling area remains concentrated above canal-containing canyons without a consistent spatial pattern. In the net warming regions (Fig. 12d), the spatial pattern is more fragmented, lacking the coherent structures observed in Area I. Therefore, without a cross-canyon vortex, cool air remains concentrated near the water surface, where surface flux dominates the local cooling budget. Advection accounts for a smaller and spatially inconsistent share of the cooling, reflecting limited lateral and vertical redistribution compared to the perpendicular configuration, such that the canal-induced air temperature reduction at pedestrian level ($z/z_H \leq 0.5$) remains largely confined to locations directly above or immediately adjacent to the water surface. This qualitative contrast between Area I and Area II is preserved across the sensitivity simulations, where the advection contribution varies by approximately 6.3% in net cooling regions and 9.5% in net warming regions per Kelvin, comparable to the sensitivity observed in Area I yet without altering the conclusion that advective redistribution is fundamentally weaker in the parallel wind-canal configuration (Figure S7).

6.2. Implications for urban blue space design

The present simulations, based on Amsterdam's historic canal morphology under a single anticyclonic summer day, directly demonstrate that wind-canal orientation governs whether canal cooling reaches pedestrians or remains confined above the water surface. Under perpendicular wind conditions, organized cross-canal circulation advects cooled air into adjacent street canyons, producing pedestrian-level temperature reductions on the order of 0.5 to 1.5°C and a vertical cooling extent reaching $z/z_H = 2$ to 3. Under parallel wind conditions, turbulent exchange dominates and cooling remains largely confined above the canal with limited lateral propagation. While these magnitudes are case-specific, the orientation dependence itself establishes a physically general hierarchy of cooling effectiveness that should be the starting point for any canal-based urban heat mitigation strategy.

Drawing directly from these case-specific results, three practical design considerations emerge at the street and corridor scale. First, new blue–green corridors should be oriented to intercept dominant warm-season wind directions, maximizing the probability that cooled air is advected into adjacent street canyons rather than remaining above the water. Second, where canal alignment is fixed, building openings and street-level ventilation pathways perpendicular to the canal axis can extend the functional cooling zone without requiring changes to the water network itself. Third, infill development adjacent to canals should be evaluated for its impact on canyon ventilation: raising building heights, narrowing streets, or introducing building masses perpendicular to prevailing winds can substantially degrade the advective cooling pathway even without modifying the water body. Additionally, the simulated perpendicular-wind case reveals a spatial asymmetry relevant to pedestrian comfort: leeward pedestrians experience up to 1.5°C more cooling than windward pedestrians along the same canal, and public pathway placement should account for this heterogeneity.

Generalizing beyond the specific case, cooling performance at the block and neighborhood scale depends on how well the surrounding urban fabric transmits canal-cooled air into the wider street network, a principle applicable to any canal-integrated city. Building massing, block permeability, and street connectivity collectively determine whether a cool-air plume disperses efficiently or is rapidly diluted by turbulent mixing. In compact, well-connected grids where short inter-canal distances and permeable block edges create successive canal-street-canal pathways, advective cooling can compound across multiple water bodies, producing neighborhood-scale relief beyond what any single canal achieves in isolation. In superblock layouts or morphologies with long uninterrupted building fronts, even a strongly cooled canal may fail to propagate cooling more than one to two block widths. Canal placement should therefore be considered as part of a block-scale ventilation network in which canal orientation, street connectivity, and building massing are co-optimized for cooling dispersion, regardless of the specific urban morphology. The idealized simulation conducted for grid-sensitivity purposes (Section 2.3) uses surface properties representative of the analyzed canal districts and a prescribed perpendicular wind-canal configuration; the resulting vorticity structures and near-surface temperature ranges are consistent with those in the realistic domain, suggesting that the orientation-dependent cooling hierarchy identified here is not confined to Amsterdam's specific canal geometry.

At the broadest scale, and independently of any specific morphological context, a fundamental constraint facing canal-based cooling strategies is that the wind conditions most favorable for cooling, calm anticyclonic flow aligned with the canal axis, are rarely the climatologically dominant conditions in mid-latitude cities. Prevailing winds under non-heatwave conditions are often poorly aligned with existing canal networks, meaning canals operate in the less efficient parallel-wind configuration for much of the warm season. Yet it is precisely under the infrequent calm anticyclonic regime that daytime canyon layer urban heat island intensity is strong (Steeneveld et al., 2011), making canal cooling most effective exactly when thermal stress is most severe. This alignment between cooling potential and thermal need is a general asset of canal systems that extends beyond any single case study. The governing role of wind is not unique to canals; windcatcher systems in arid urban canyons similarly demonstrate that airflow enhancement is a prerequisite for pedestrian-level heat mitigation (Kachmar et al., 2025). Beyond the warm season, open water surfaces that facilitate summer cooling may amplify cold discomfort under strong winter winds (Oke et al., 2017), and balancing these seasonal trade-offs requires site-specific wind-rose analysis rather than a blanket recommendation for canal integration.

Finally, placing these findings in the broader context of urban nature-based solutions, the cooling magnitudes demonstrated here are comparable to those reported for green infrastructure, suggesting blue and green interventions are complementary rather than competing strategies. Canal cooling acts principally through sensible heat flux reduction and advective redistribution, whereas green infrastructure combines solar shading with evapotranspiration and aerodynamic drag (Li & Wang, 2018). Street trees yield canyon-averaged air temperature reductions of approximately 0.5°C (Mun et al., 2024), with a global synthesis finding temperate-climate pedestrian-level reductions well below 2°C despite larger mean radiant temperature effects (H. Li et al., 2024). Under low-radiation conditions, the shading benefit of trees disappears, yet aerodynamic drag retains a thermal comfort benefit that open water cannot provide, while canals maintain their sensible heat flux advantage regardless of sky condition. Combined blue–green configurations can therefore exploit the complementary strengths of both systems, offering more balanced year-round performance than either alone. The turbulent-advective decomposition framework demonstrated here provides a transferable diagnostic tool for evaluating such combined configurations across diverse urban morphologies.

6.3. Limitations and outlook

The present study has a few limitations that bound the generality of its findings. The simulations represent a single summer day under specific meteorological conditions, namely clear sky and moderate wind speed, and are restricted to two wind-canal orientations with a fixed canyon geometry and prescribed water surface temperature. These choices provide controlled mechanistic insight but leave open how cooling effectiveness varies across meteorological regimes, canyon configurations, wind-canal angles, and coupled water-atmosphere feedbacks. The specific quantitative results reported here, including cooling magnitudes, advective contribution percentages, and the spatial extent of cooling, are case-specific to this meteorological and morphological setting and should not be directly extrapolated to other conditions. The underlying physical mechanisms and the heat-transport decomposition framework, however, are generalizable and transferable to other urban water-body configurations.

Several sources of uncertainty affect the quantitative conclusions and should be considered when interpreting the results. First, the mesoscale WRF simulation provides lateral boundary conditions through one-way nesting, capturing the large-scale synoptic environment but not sub-mesoscale boundary-layer variability; errors in the WRF surface-layer parameterization may therefore propagate into the LES domain. Second, urban surface properties including albedo, roughness length, and heat capacity were derived from GIS datasets and literature values, carrying inherent parameter uncertainty; leaf area index for street trees is particularly uncertain, and the absence of explicit anthropogenic heat release may lead to modest underestimation of sensible heat in densely built areas. Third, canal water temperature was prescribed as a spatially uniform, temporally constant 295 K, introducing uncertainty in the absolute magnitude of both turbulent exchange and advective redistribution, since the sensible heat flux is directly proportional to the water-air temperature contrast; sensitivity simulations at 294 K and 296 K confirm that the key findings are robust within this range. Nevertheless, the prescribed water temperature neglects diurnal variation, thermal stratification, shortwave penetration, and bottom heat exchange, which could modulate the intensity and temporal-spatial variation of water–atmosphere heat exchange. The 1 K sensitivity range tested here is intended to partially bracket this uncertainty, though future studies with coupled water–atmosphere models would better constrain these effects. Finally, the advective heat flux is a diagnostically derived quantity sensitive to the definition of the control volume, the choice of reference height, and the vertical layer thickness used in the $\mathrm{W\,m^{-2}}$ conversion; the reported 60 to 80% advective contribution should therefore be interpreted as an order-of-magnitude indicator of the relative importance of advective versus turbulent pathways rather than a precise measurement.

Future research should systematically investigate how diverse urban morphologies and street canyon configurations interact with water bodies to affect cooling effectiveness. The current analysis examines two wind-canal orientations at a specific time step with realistic canyon geometry, revealing two different cooling patterns. However, the relationship between canyon geometry and cooling effectiveness is sophisticated and needs further investigation. While narrow canyons exhibit stronger vortex circulation, concentrating cooling on the upwind side, very high buildings relative to street width (low canyon aspect ratio) may trap cool air within canyons, limiting vertical transport and spatial extent of cooling benefits (J. Li et al., 2024). Optimal canyon configurations likely depend on balancing vortex strength (favored by moderate canyon aspect ratio) and vertical ventilation. Future parametric studies should also quantify cooling effectiveness across wind-canal angles, canyon aspect ratios, building heights, and street widths to determine whether transitions are linear, nonlinear, or exhibit threshold behaviors (Zhao et al., 2020). Incorporating diurnal wind shifts would capture temporal variability in cooling effectiveness as local circulation systems modify wind patterns. Such comprehensive investigations would establish generalized design principles applicable beyond example geometries, informing flexible guidelines that optimize canal placement and urban morphology configurations for maximum cooling benefits across diverse urban contexts.

Incorporating coupled water-atmosphere modeling would enable investigation of feedback processes and optimization of water body design parameters, though such comprehensive modeling is beyond the scope of the current study and represents a substantial research undertaking requiring community-wide effort. The current prescribed surface temperature boundary conditions isolate atmospheric response to a given water temperature, providing clear mechanistic insight into flow-mediated cooling redistribution. Future coupled models would reveal how atmospheric conditions modify water temperature through surface energy balance (Chen et al., 2025), and would address critical design parameters including water depth requirements for maintaining stable surface temperatures, differences in cooling effectiveness between flowing versus stagnant water bodies, and the impact of canal shading by buildings or vegetation. Spatially explicit water temperature modeling would capture horizontal gradients from differential solar heating, inflow/outflow characteristics, and interaction with surrounding surfaces, enabling comprehensive optimization of canal design parameters, including flow rate, depth, and shading strategies. These advances would require coordinated efforts combining expertise in urban climatology, hydrology, and urban design, alongside extensive field observations to validate coupled model performance across diverse urban contexts.

7. Conclusions

This study employed the PALM4U model with LES to investigate the mechanisms through which urban canals modify sensible heat partitioning and heat transport in Amsterdam, Netherlands, a dense historic center. Model evaluation against eddy covariance flux tower and urban weather station observations demonstrated strong performance for sensible heat flux (IoA = 0.94), net radiation (IoA = 1.00), and near surface air temperature (IoA = 0.72), establishing LES as a reliable tool for quantifying urban surface-atmosphere energy exchange.

By decomposing thermal effects into turbulent and advective components through controlled with-canal and without-canal experiments, we revealed that canal cooling effectiveness depends fundamentally on wind direction with respect to canal orientation. When wind flows perpendicular to canals, mechanically-driven canyon vortices redistribute cool air from the water surface to surrounding areas, with advection accounting for 60 to 80% of the total cooling effect over adjacent pavement and above the canopy. This redistribution extends the spatial footprint of cooling asymmetrically, propagating vertically to 2 to 3 building heights and horizontally to adjacent canyons lacking water features. When wind flows parallel to canals, the absence of a cross-canyon vortex limits lateral and vertical redistribution, leaving cooling concentrated near the water surface and driven predominantly by local sensible heat flux reduction. In this configuration, advection accounts for a smaller and spatially inconsistent share of the cooling budget, resulting in more localized thermal benefits despite comparable cooling intensity directly above the water surface. Importantly, advection redistributes heat within the urban canopy rather than removing more heat from the system overall: it changes where cooling is felt, not how much cooling occurs.

These physical insights offer guidance for urban blue space planning, though they should be interpreted within the scope of the present case. Historical canal systems originally designed for transportation may deliver spatially confined and relatively uniform thermal benefits where their orientation is unfavorable relative to prevailing summer winds, as cooling tends to remain near the water surface. Where canals are oriented perpendicular to prevailing winds, cooling is redistributed more heterogeneously across the urban fabric, benefiting some areas more strongly while reducing benefits in others, rather than increasing overall cooling intensity. In practical terms, this suggests that aligning blue–green infrastructure layout with prevailing summer wind directions, and treating canal-axis orientation as a design variable alongside canal width and adjacent building height, can help direct cooling toward pedestrian spaces where it is most needed. The strong spatial heterogeneity we found, with temperature differences up to 1.5°C within individual street canyons, underlines that the thermal benefits of blue infrastructure are highly location-dependent within the urban canyon and cannot be assumed uniform.

At the same time, these conclusions are drawn from a single representative summer day under anticyclonic conditions and from Amsterdam's distinctive semi-circular canal morphology and dense historic fabric. The specific values reported here should therefore be regarded as case-specific rather than universal, and the underlying mechanism, namely that wind-canal orientation governs the spatial distribution of cooling through canyon-scale circulation, is expected to be more broadly transferable than the precise magnitudes. Caution is warranted when extrapolating to cities with different canal geometries, wider rivers, grid-based street layouts, or different climatic regimes.

This research advances understanding of urban water body cooling beyond empirical temperature assessments by quantifying the relative contributions of vertical turbulent exchange versus horizontal advective transport. The finding that advection can either enhance or limit cooling depending on flow structure challenges simplified representations of water body effects in urban climate models. Future work should test the robustness of these findings across diverse meteorological conditions and seasons, investigate the full spectrum of wind-canal angles and contrasting urban morphologies, and develop coupled water-atmosphere models to optimize design parameters, including canal depth, flow rate, and shading strategies.

CRediT authorship contribution statement

Xuan Chen: Writing – original draft, Visualization, Software, Methodology, Investigation, Formal analysis, Data curation, Conceptualization. **Srinidhi Gadde:** Writing – review & editing, Software, Methodology, Conceptualization. **Gert-Jan Steeneveld:** Writing – review & editing, Resources. **Remko Uijlenhoet:** Writing – review & editing, Resources, Funding acquisition.

Declaration of competing interest

The authors declare that they have no known competing financial interests or personal relationships that could have appeared to influence the work reported in this paper.

Appendix A. Supplementary data

Supplementary material related to this article can be found online at https://doi.org/10.1016/j.scs.2026.107804.

Data availability

Data will be made available on request.

References

Amaripadath, D., & Sailor, D. J. (2025). Systematic review on cooling benefits of landscape strategies for urban thermal environments in the United States. *Sustainable Cities and Society*, *129*, Article 106497. http://dx.doi.org/10.1016/j.scs.2025.106497, URL https://www.sciencedirect.com/science/article/pii/S2210670725003737.

Amini, S., Huerta, A., Franke, J., Brugnara, Y., Caluwaerts, S., Anet, J., Savić, S., Gubler, M., Steeneveld, G.-J., Chapman, L., Meier, F., Dubreuil, V., Christen, A., Zeeman, M., Lalić, B., Schlögl, S., Käyhkö, J., Azadfar, A., & Brönnimann, S. (2026). Comprehensive compilation and quality assessment of street-level urban air temperature measurements across European networks. *Scientific Data*, http://dx.doi.org/10.1038/s41597-026-06804-4, URL https://www.nature.com/articles/s41597-026-06804-4.

Ampatzidis, P., & Kershaw, T. (2020). A review of the impact of blue space on the urban microclimate. *Science of the Total Environment*, *730*, Article 139068. http://dx.doi.org/10.1016/j.scitotenv.2020.139068, URL https://www.sciencedirect.com/science/article/pii/S0048969720325857.

Anders, J., Schubert, S., Sauter, T., Tunn, S., Schneider, C., & Salim, M. (2023). Modelling the impact of an urban development project on microclimate and outdoor thermal comfort in a mid-latitude city. *Energy and Buildings*, *296*, Article 113324. http://dx.doi.org/10.1016/j.enbuild.2023.113324, URL https://www.sciencedirect.com/science/article/pii/S0378778823005546.

Chen, X., Gadde, S., Droste, A., Steeneveld, G.-J., Coenders-Gerrits, M., & Uijlenhoet, R. (2026). Assessing the role of urban blue space in summer outdoor thermal regulation in northwestern Europe: A hectometric Weather Research and Forecasting modelling on idealized urban landscape. *Quarterly Journal of the Royal Meteorological Society*, *n/a*(n/a), Article e70128. http://dx.doi.org/10.1002/qj.70128, URL https://onlinelibrary.wiley.com/doi/abs/10.1002/qj.70128, _eprint: https://rmets.onlinelibrary.wiley.com/doi/pdf/10.1002/qj.70128.

Chen, X., Wang, H., & Yang, J. (2024). Effect of green blue spaces on the urban thermal environment: A field study in Hong Kong. *Urban Climate*, *55*, Article 101912. http://dx.doi.org/10.1016/j.uclim.2024.101912, URL https://www.sciencedirect.com/science/article/pii/S2212095524001081.

Chen, X., van der Werf, J. A., Droste, A., Coenders-Gerrits, M., & Uijlenhoet, R. (2025). Barriers to urban hydrometeorological simulation: a review. *Hydrology and Earth System Sciences*, *29*(15), 3447–3480. http://dx.doi.org/10.5194/hess-29-3447-2025, URL https://hess.copernicus.org/articles/29/3447/2025/.

Cobra-Groeninzicht (2025). Tree data.

Crank, P. J., Sailor, D. J., Ban-Weiss, G., & Taleghani, M. (2018). Evaluating the ENVI-met microscale model for suitability in analysis of targeted urban heat mitigation strategies. *Urban Climate*, *26*, 188–197. http://dx.doi.org/10.1016/j.uclim.2018.09.002, URL https://www.sciencedirect.com/science/article/pii/S2212095518301007.

Crawford, B., Grimmond, C. S. B., Ward, H. C., Morrison, W., & Kotthaus, S. (2017). Spatial and temporal patterns of surface–atmosphere energy exchange in a dense urban environment using scintillometry. *Quarterly Journal of the Royal Meteorological Society*, *143*(703), 817–833. http://dx.doi.org/10.1002/qj.2967, URL https://onlinelibrary.wiley.com/doi/abs/10.1002/qj.2967, _eprint: https://rmets.onlinelibrary.wiley.com/doi/pdf/10.1002/qj.2967.

Dang, M., Dobbelsteen, A. v. d., & Voskuilen, P. (2024). A parametric modelling approach for energy retrofitting heritage buildings: The case of amsterdam city centre. *Energies*, *17*(5), http://dx.doi.org/10.3390/en17050994, URL https://www.mdpi.com/1996-1073/17/5/994.

Deardorff, J. W. (1980). Stratocumulus-capped mixed layers derived from a three-dimensional model. *Boundary-Layer Meteorology*, *18*(4), 495–527. http://dx.doi.org/10.1007/BF00119502, URL https://doi.org/10.1007/BF00119502.

Foken, T., Göockede, M., Mauder, M., Mahrt, L., Amiro, B., & Munger, W. (2004). Post-field data quality control. In *Handbook of micrometeorology: a guide for surface flux measurement and analysis* (pp. 181–208). Springer.

Fröhlich, D., & Matzarakis, A. (2020). Calculating human thermal comfort and thermal stress in the PALM model system 6.0. *Geoscientific Model Development*, *13*(7), 3055–3065. http://dx.doi.org/10.5194/gmd-13-3055-2020, URL https://gmd.copernicus.org/articles/13/3055/2020/.

Gadde, S. N., Stieren, A., & Stevens, R. J. (2021). Large-eddy simulations of stratified atmospheric boundary layers: Comparison of different subgrid models. *Boundary-Layer Meteorology*, *178*(3), 363–382. http://dx.doi.org/10.1007/s10546-020-00570-5.

Galalizadeh, S., Morrison-Saunders, A., Horwitz, P., Silberstein, R., & Blake, D. (2024). The cooling impact of urban greening: A systematic review of methodologies and data sources. *Urban Forestry & Urban Greening*, *95*, Article 128157. http://dx.doi.org/10.1016/j.ufug.2023.128157, URL https://www.sciencedirect.com/science/article/pii/S161886672300328X.

Gehrke, K. F., Sühring, M., & Maronga, B. (2021). Modeling of land–surface interactions in the PALM model system 6.0: Land surface model description, first evaluation, and sensitivity to model parameters. *Geoscientific Model Development*, *14*(8), 5307–5329. http://dx.doi.org/10.5194/gmd-14-5307-2021, URL https://gmd.copernicus.org/articles/14/5307/2021/.

Geletič, J., Lehnert, M., Resler, J., Krč, P., Bureš, M., Urban, A., & Krayenhoff, E. S. (2023). Heat exposure variations and mitigation in a densely populated neighborhood during a hot day: Towards a people-oriented approach to urban climate management. *Building and Environment*, *242*, Article 110564. http://dx.doi.org/10.1016/j.buildenv.2023.110564, URL https://www.sciencedirect.com/science/article/pii/S0360132323005917.

Gronemeier, T., Surm, K., Harms, F., Leitl, B., Maronga, B., & Raasch, S. (2021). Evaluation of the dynamic core of the PALM model system 6.0 in a neutrally stratified urban environment: comparison between LES and wind-tunnel experiments. *Geoscientific Model Development*, *14*(6), 3317–3333. http://dx.doi.org/10.5194/gmd-14-3317-2021, URL https://gmd.copernicus.org/articles/14/3317/2021/.

Guo, X., Yan, C., & Miao, S. (2023). A rapid modeling method for urban microscale meteorology and its applications. *Science China Earth Sciences*, *66*(10), 2224–2238. http://dx.doi.org/10.1007/s11430-022-1160-6, URL https://doi.org/10.1007/s11430-022-1160-6.

Heldens, W., Burmeister, C., Kanani-Sühring, F., Maronga, B., Pavlik, D., Sühring, M., Zeidler, J., & Esch, T. (2020). Geospatial input data for the PALM model system 6.0: Model requirements, data sources and processing. *Geoscientific Model Development*, *13*(11), 5833–5873. http://dx.doi.org/10.5194/gmd-13-5833-2020, URL https://gmd.copernicus.org/articles/13/5833/2020/.

Hersbach, H., Bell, B., Berrisford, P., Hirahara, S., Horányi, A., Muñoz-Sabater, J., Nicolas, J., Peubey, C., Radu, R., Schepers, D., Simmons, A., Soci, C., Abdalla, S., Abellan, X., Balsamo, G., Bechtold, P., Biavati, G., Bidlot, J., Bonavita, M., ... Thépaut, J. N. (2020). The ERA5 global reanalysis. *Quarterly Journal of the Royal Meteorological Society*, *146*(730), 1999–2049. http://dx.doi.org/10.1002/qj.3803, URL https://onlinelibrary.wiley.com/doi/abs/10.1002/qj.3803, _eprint: https://rmets.onlinelibrary.wiley.com/doi/pdf/10.1002/qj.3803.

Hollósi, B., Žuvela-Aloise, M., Neureiter, A., Frießenbichler, M., Auferbauer, P., Feigl, J., Hahn, C., & Kolejka, T. (2024). Capability of the building-resolving PALM model system to capture micrometeorological characteristics of an urban environment in Vienna, Austria. *City and Environment Interactions*, *23*, Article 100152. http://dx.doi.org/10.1016/j.cacint.2024.100152, URL https://www.sciencedirect.com/science/article/pii/S2590252024000126.

Iacono, M. J., Delamere, J. S., Mlawer, E. J., Shephard, M. W., Clough, S. A., & Collins, W. D. (2008). Radiative forcing by long-lived greenhouse gases: Calculations with the AER radiative transfer models. *Journal of Geophysical Research: Atmospheres*, *113*(D13), http://dx.doi.org/10.1029/2008JD009944, URL https://onlinelibrary.wiley.com/doi/abs/10.1029/2008JD009944, _eprint: https://agupubs.onlinelibrary.wiley.com/doi/pdf/10.1029/2008JD009944.

Jacobs, C., Klok, L., Bruse, M., Cortesão, J., Lenzholzer, S., & Kluck, J. (2020). Are urban water bodies really cooling? *Urban Climate*, *32*, Article 100607. http://dx.doi.org/10.1016/j.uclim.2020.100607, URL https://www.sciencedirect.com/science/article/pii/S2212095519301002.

Jansen, F. A., Jongen, H. J., Jacobs, C. M. J., Bosveld, F. C., Buzacott, A. J. V., Heusinkveld, B. G., Kruijt, B., van der Molen, M., Moors, E., Steeneveld, G.-J., van der Tol, C., van der Velde, Y., Voortman, B., Uijlenhoet, R., & Teuling, A. J. (2023). Land cover control on the drivers of evaporation and sensible heat fluxes: An observation-based synthesis for the Netherlands. *Water Resources Research*, *59*(11), Article e2022WR034361. http://dx.doi.org/10.1029/2022WR034361, URL https://onlinelibrary.wiley.com/doi/abs/10.1029/2022WR034361, _eprint: https://agupubs.onlinelibrary.wiley.com/doi/pdf/10.1029/2022WR034361.

Järvi, L., Rannik, Ü., Kokkonen, T. V., Kurppa, M., Karppinen, A., Kouznetsov, R. D., Rantala, P., Vesala, T., & Wood, C. R. (2018). Uncertainty of eddy covariance flux measurements over an urban area based on two towers. *Atmospheric Measurement Techniques*, *11*(10), 5421–5438. http://dx.doi.org/10.5194/amt-11-5421-2018, URL https://amt.copernicus.org/articles/11/5421/2018/.

Kachmar, H., Younes, J., & Ghaddar, N. (2025). Effectiveness of outdoor windcatcher and mist cooling in mitigating urban heat and improving pedestrian thermal comfort. *Sustainable Cities and Society*, *132*, Article 106838. http://dx.doi.org/10.1016/j.scs.2025.106838, URL https://www.sciencedirect.com/science/article/pii/S2210670725007115.

KNMI (2022). KNMI - Augustus 2022. URL https://www.knmi.nl/nederland-nu/klimatologie/maand-en-seizoensoverzichten/2022/augustus.

Koopmans, S., van Haren, R., Theeuwes, N., Ronda, R., Uijlenhoet, R., Holtslag, A. A. M., & Steeneveld, G.-J. (2023). The set-up and evaluation of fine-scale data assimilation for the urban climate of Amsterdam. *Quarterly Journal of the Royal Meteorological Society*, *149*(750), 171–191. http://dx.doi.org/10.1002/qj.4401, URL https://onlinelibrary.wiley.com/doi/abs/10.1002/qj.4401, _eprint: https://rmets.onlinelibrary.wiley.com/doi/pdf/10.1002/qj.4401.

Krč, P., Belda, M., Bureš, M., Eben, K., Geletič, J., Radović, J., Řezníček, H., & Resler, J. (2025). PALM-meteo 2.6: Processor of PALM meteorological input data. *EGUsphere*, 1–32. http://dx.doi.org/10.5194/egusphere-2025-4120, URL https://egusphere.copernicus.org/preprints/2025/egusphere-2025-4120/.

Krč, P., Resler, J., Sühring, M., Schubert, S., Salim, M. H., & Fuka, V. (2021). Radiative Transfer Model 3.0 integrated into the PALM model system 6.0. *Geoscientific Model Development*, *14*(5), 3095–3120. http://dx.doi.org/10.5194/gmd-14-3095-2021, URL https://gmd.copernicus.org/articles/14/3095/2021/.

Kumar, P., Debele, S. E., Khalili, S., Halios, C. H., Sahani, J., Aghamohammadi, N., Andrade, M. d., Athanassiadou, M., Bhui, K., Calvillo, N., Cao, S.-J., Coulon, F., Edmondson, J. L., Fletcher, D., Freitas, E. D. d., Guo, H., Hort, M. C., Katti, M., Kjeldsen, T. R., ... Jones, L. (2024). Urban heat mitigation by green and blue infrastructure: Drivers, effectiveness, and future needs. *The Innovation*, *5*(2), http://dx.doi.org/10.1016/j.xinn.2024.100588, URL https://www.cell.com/the-innovation/abstract/S2666-6758(24)00026-2.

Letzel, M. O., Krane, M., & Raasch, S. (2008). High resolution urban large-eddy simulation studies from street canyon to neighbourhood scale. *Atmospheric Environment*, *42*(38), 8770–8784. http://dx.doi.org/10.1016/j.atmosenv.2008.08.001, URL https://www.sciencedirect.com/science/article/pii/S1352231008007036.

Li, Q., & Wang, Z.-H. (2018). Large-eddy simulation of the impact of urban trees on momentum and heat fluxes. In *Honoring W.J. Massman's discoveries: Bringing physics to agriculture*: *Agricultural and Forest Meteorology*, In *Honoring W.J. Massman's discoveries: Bringing physics to agriculture*: *255*, 44–56. http://dx.doi.org/10.1016/j.agrformet.2017.07.011.URL https://www.sciencedirect.com/science/article/pii/S0168192317302277,

Li, J., You, W., Peng, Y., & Ding, W. (2024). Exploring the potential of the aspect ratio to predict flow patterns in actual urban spaces for ventilation design by comparing the idealized and actual canyons. *Sustainable Cities and Society*, *102*, Article 105214. http://dx.doi.org/10.1016/j.scs.2024.105214, URL https://www.sciencedirect.com/science/article/pii/S221067072400043X.

Li, H., Zhao, Y., Wang, C., Ürge-Vorsatz, D., Carmeliet, J., & Bardhan, R. (2024). Cooling efficacy of trees across cities is determined by background climate, urban morphology, and tree trait. *Communications Earth & Environment*, *5*(1), 754. http://dx.doi.org/10.1038/s43247-024-01908-4, URL https://www.nature.com/articles/s43247-024-01908-4.

Lieber, J., Chen, X., Chen, L., & Yang, J. (2025). Comparative analysis of microclimate simulations: Assessing the single-layer urban canopy model and ENVI-met in Hong Kong. *Urban Climate*, *64*, Article 102621. http://dx.doi.org/10.1016/j.uclim.2025.102621, URL https://www.sciencedirect.com/science/article/pii/S2212095525003372.

Linden, L. v. d., Hogan, P., Maronga, B., Hagemann, R., & Bechtel, B. (2023). Crowdsourcing air temperature data for the evaluation of the urban microscale model PALM—A case study in central Europe. *PLOS Climate*, *2*(8), Article e0000197. http://dx.doi.org/10.1371/journal.pclm.0000197, URL https://journals.plos.org/climate/article?id=10.1371/journal.pclm.0000197.

Liu, X., He, B., Guo, L., Huang, L., & Chen, D. (2020). Similarities and differences in the mechanisms causing the European summer heatwaves in 2003, 2010, and 2018. *Earth's Future*, *8*(4), Article e2019EF001386. http://dx.doi.org/10.1029/2019EF001386, URL https://onlinelibrary.wiley.com/doi/abs/10.1029/2019EF001386, _eprint: https://agupubs.onlinelibrary.wiley.com/doi/pdf/10.1029/2019EF001386.

Lorenz, R., Stalhandske, Z., & Fischer, E. M. (2019). Detection of a climate change signal in extreme heat, heat stress, and cold in Europe from observations. *Geophysical Research Letters*, *46*(14), 8363–8374. http://dx.doi.org/10.1029/2019GL082062, URL https://onlinelibrary.wiley.com/doi/abs/10.1029/2019GL082062, _eprint: https://agupubs.onlinelibrary.wiley.com/doi/pdf/10.1029/2019GL082062.

Manteghi, G., Limit, H., & Remaz, D. (2015). Water bodies an urban microclimate: A review. *Modern Applied Science*, *9*(6), p1. http://dx.doi.org/10.5539/mas.v9n6p1, URL https://ccsenet.org/journal/index.php/mas/article/view/42398.

Maronga, B., Banzhaf, S., Burmeister, C., Esch, T., Forkel, R., Fröhlich, D., Fuka, V., Gehrke, KF., Geleti, J., Giersch, S., Gronemeier, T., Groß, G., Heldens, W., Hellsten, A., Hoffmann, F., Inagaki, A., Kadasch, E., Kanani-Sühring, F., Ketelsen, K., ... Raasch, S. (2020). Overview of the PALM model system 6.0. *Geoscientific Model Development*, *13*(3), 1335–1372. http://dx.doi.org/10.5194/gmd-13-1335-2020, URL https://gmd.copernicus.org/articles/13/1335/2020/.

Maronga, B., Gryschka, M., Heinze, R., Hoffmann, F., Kanani-Sühring, F., Keck, M., Ketelsen, K., Letzel, M. O., Sühring, M., & Raasch, S. (2015). The parallelized large-eddy simulation model (PALM) version 4.0 for atmospheric and oceanic flows: Model formulation, recent developments, and future perspectives. *Geoscientific Model Development*, *8*(8), 2515–2551. http://dx.doi.org/10.5194/gmd-8-2515-2015, URL https://gmd.copernicus.org/articles/8/2515/2015/gmd-8-2515-2015.html.

Mlawer, E. J., Taubman, S. J., Brown, P. D., Iacono, M. J., & Clough, S. A. (1997). Radiative transfer for inhomogeneous atmospheres: RRTM, a validated correlated-k model for the longwave. *Journal of Geophysical Research: Atmospheres*, *102*(D14), 16663–16682. http://dx.doi.org/10.1029/97JD00237, URL https://onlinelibrary.wiley.com/doi/abs/10.1029/97JD00237, _eprint: https://agupubs.onlinelibrary.wiley.com/doi/pdf/10.1029/97JD00237.

Mun, D., Kang, G., Yang, M., & Kim, J. (2024). How trees' drag and cooling effects influence airflow and temperature distributions around a street canyon. *Building and Environment*, *264*, Article 111913. http://dx.doi.org/10.1016/j.buildenv.2024.111913, URL https://www.sciencedirect.com/science/article/pii/S0360132324007558.

Nordbo, A., Järvi, L., & Vesala, T. (2012). Revised eddy covariance flux calculation methodologies – effect on urban energy balance. *Tellus B: Chemical and Physical Meteorology*, *64*(1), 18184. http://dx.doi.org/10.3402/tellusb.v64i0.18184, URL https://doi.org/10.3402/tellusb.v64i0.18184, _eprint: https://doi.org/10.3402/tellusb.v64i0.18184.

Offerle, B., Eliasson, I., Grimmond, C. S. B., & Holmer, B. (2007). Surface heating in relation to air temperature, wind and turbulence in an urban street canyon. *Boundary-Layer Meteorology*, *122*(2), 273–292. http://dx.doi.org/10.1007/s10546-006-9099-8, URL https://doi.org/10.1007/s10546-006-9099-8.

Oke, T. R. (1988). Street design and urban canopy layer climate. *Energy and Buildings*, *11*(1), 103–113. http://dx.doi.org/10.1016/0378-7788(88)90026-6, URL https://www.sciencedirect.com/science/article/pii/0378778888900266.

Oke, T. R., Mills, G., Christen, A., & Voogt, J. A. (2017). *Urban climates*. Cambridge: Cambridge University Press, http://dx.doi.org/10.1017/9781139016476, URL https://www.cambridge.org/core/books/urban-climates/A02424592E1C7F9B9CD69DAD57A5B50B.

Overheid (2023). Actueel Hoogtebestand Nederland 4. URL https://www.arcgis.com/apps/mapviewer/index.html?layers=77da2e9eeea8427aab2ac83b79097b1a, (Accessed 03 October 2025).

PDOK (2025a). Basisregistratie Adressen en Gebouwen (BAG). https://www.pdok.nl/introductie/-/article/basisregistratie-adressen-en-gebouwen-ba-1. (Accessed 03 October 2025).

PDOK (2025b). Basisregistratie Grootschalige Topografie (BGT). https://www.pdok.nl/introductie/-/article/basisregistratie-grootschalige-topografie-bgt-. (Accessed 03 October 2025).

PDOK (2025c). Luchtfoto Beeldmateriaal 8cm en 25cm RGB WMTS. https://www.pdok.nl/introductie/-/article/pdok-luchtfoto-rgb-open-. (Accessed 03 October 2025).

Peters, R., Dukai, B., Vitalis, S., van Liempt, J., & Stoter, J. (2022). Automated 3D Reconstruction of LoD2 and LoD1 Models for All 10 Million Buildings of the Netherlands. *Photogrammetric Engineering and Remote Sensing*, *88*(3), 165–170. http://dx.doi.org/10.14358/PERS.21-00032R2.

Resler, J., Krč, P., Belda, M., Juruš, P., Benešová, N., Lopata, J., Vlček, O., Damašková, D., Eben, K., Derbek, P., Maronga, B., & Kanani-Sühring, F. (2017). PALM-USM v1.0: A new urban surface model integrated into the PALM large-eddy simulation model. *Geoscientific Model Development*, *10*(10), 3635–3659. http://dx.doi.org/10.5194/gmd-10-3635-2017, URL https://gmd.copernicus.org/articles/10/3635/2017/gmd-10-3635-2017-discussion.html.

Rijkswaterstaat (2022). Waterinfo.nl: National water monitoring network data. Surface water temperature data for Amsterdam canals, accessed August 2022, https://www.rijkswaterstaat.nl/water.

Ronda, R. J., Steeneveld, G. J., Heusinkveld, B. G., Attema, J. J., & Holtslag, A. a. M. (2017). Urban finescale forecasting reveals weather conditions with unprecedented detail. *Bulletin of the American Meteorological Society*, *98*(12), 2675–2688. http://dx.doi.org/10.1175/BAMS-D-16-0297.1, URL https://journals.ametsoc.org/view/journals/bams/98/12/bams-d-16-0297.1.xml.

Saiki, E. M., Moeng, C.-H., & Sullivan, P. P. (2000). Large-eddy simulation of the stably stratified planetary boundary layer. *Boundary-Layer Meteorology*, *95*(1), 1–30. http://dx.doi.org/10.1023/A:1002428223156, URL https://doi.org/10.1023/A:1002428223156.

Salim, S. M., Cheah, S. C., & Chan, A. (2011). Numerical simulation of dispersion in urban street canyons with avenue-like tree plantings: Comparison between RANS and LES. *Building and Environment*, *46*(9), 1735–1746. http://dx.doi.org/10.1016/j.buildenv.2011.01.032.

Salim, M. H., Schubert, S., Resler, J., Krč, P., Maronga, B., Kanani-Sühring, F., Sühring, M., & Schneider, C. (2022). Importance of radiative transfer processes in urban climate models: A study based on the PALM 6.0 model system. *Geoscientific Model Development*, *15*(1), 145–171. http://dx.doi.org/10.5194/gmd-15-145-2022, URL https://gmd.copernicus.org/articles/15/145/2022/.

Skamarock, W., Klemp, J., Dudhia, J., Gill, D. O., Liu, A. Z., Berner, J., Wang, W., Powers, J. G., Duda, M. G., Barker, D., & Huang, X.-Y. (2019). *A description of the advanced research WRF model version 4.1*: *Tech rep*, National Center for Atmospheric Research (NCAR), URL https://opensky.ucar.edu/islandora/object/%3A3888.

Soulhac, L., Salizzoni, P., Cierco, F. X., & Perkins, R. (2011). The model SIRANE for atmospheric urban pollutant dispersion; part i, presentation of the model. *Atmospheric Environment*, *45*(39), 7379–7395. http://dx.doi.org/10.1016/j.atmosenv.2011.07.008, URL https://www.sciencedirect.com/science/article/pii/S1352231011007096.

Steeneveld, G. J., Koopmans, S., Heusinkveld, B. G., van Hove, L. W. A., & Holtslag, A. A. M. (2011). Quantifying urban heat island effects and human comfort for cities of variable size and urban morphology in the Netherlands. *Journal of Geophysical Research: Atmospheres*, *116*(D20), http://dx.doi.org/10.1029/2011JD015988, URL https://onlinelibrary.wiley.com/doi/abs/10.1029/2011JD015988, _eprint: https://agupubs.onlinelibrary.wiley.com/doi/pdf/10.1029/2011JD015988.

Stefanon, M., D'Andrea, F., & Drobinski, P. (2012). Heatwave classification over Europe and the Mediterranean region. *Environmental Research Letters*, *7*(1), Article 014023. http://dx.doi.org/10.1088/1748-9326/7/1/014023, URL https://doi.org/10.1088/1748-9326/7/1/014023.

Tominaga, Y., Sato, Y., & Sadohara, S. (2015). CFD simulations of the effect of evaporative cooling from water bodies in a micro-scale urban environment: Validation and application studies. *Sustainable Cities and Society*, *19*, 259–270. http://dx.doi.org/10.1016/j.scs.2015.03.011, URL https://www.sciencedirect.com/science/article/pii/S2210670715000396.

Toparlar, Y., Blocken, B., Maiheu, B., & Van Heijst, G. (2017). A review on the CFD analysis of urban microclimate. *Renewable and Sustainable Energy Reviews*, *80*, 1613–1640. http://dx.doi.org/10.1016/j.rser.2017.05.248, URL https://linkinghub.elsevier.com/retrieve/pii/S1364032117308924.

UNESCO World Heritage Centre (2010). Seventeenth-century Canal Ring Area of amsterdam inside the singelgracht. URL https://whc.unesco.org/en/list/1349/, UNESCO World Heritage List.

van der Meer, W., Zantinge, F., & Steeneveld, G. J. (2025). Urban fluxes for free: Estimating urban turbulent surface fluxes from crowdsourced meteorological canyon layer observations. *City and Environment Interactions*, *27*, Article 100201. http://dx.doi.org/10.1016/j.cacint.2025.100201, URL https://www.sciencedirect.com/science/article/pii/S2590252025000157.

Vogel, J., Afshari, A., Chockalingam, G., & Stadler, S. (2022). Evaluation of a novel WRF/PALM-4U coupling scheme incorporating a roughness-corrected surface layer representation. *Urban Climate*, *46*, Article 101311. http://dx.doi.org/10.1016/j.uclim.2022.101311, URL https://www.sciencedirect.com/science/article/pii/S2212095522002292.

Wang, Q., Adiku, S., Tenhunen, J., & Granier, A. (2005). On the relationship of NDVI with leaf area index in a deciduous forest site. *Remote Sensing of Environment*, *94*(2), 244–255. http://dx.doi.org/10.1016/j.rse.2004.10.006, URL https://www.sciencedirect.com/science/article/pii/S0034425704003232.

Wang, B., Zeng, L., Zhang, X., Fu, Y., Qian, X., Guo, Y., & Wen, L. (2025). Computational fluid dynamics investigation of evaporation modeling and microclimate cooling effects of urban water bodies. *Physics of Fluids*, *37*(12), Article 125164. http://dx.doi.org/10.1063/5.0304862, URL https://doi.org/10.1063/5.0304862.

Wicker, L. J., & Skamarock, W. C. (2002). Time-splitting methods for elastic models using forward time schemes. *Monthly Weather Review*, *130*(8), 2088–2097. http://dx.doi.org/10.1175/1520-0493(2002)130<2088:TSMFEM>2.0.CO;2, URL https://journals.ametsoc.org/view/journals/mwre/130/8/1520-0493_2002_130_2088_tsmfem_2.0.co_2.xml.

Williamson, J. H. (1980). Low-storage Runge-Kutta schemes. *Journal of Computational Physics*, *35*(1), 48–56. http://dx.doi.org/10.1016/0021-9991(80)90033-9, URL https://www.sciencedirect.com/science/article/pii/0021999180900339.

Willmott, C. J., Ackleson, S. G., Davis, R. E., Feddema, J. J., Klink, K. M., Legates, D. R., O'Donnell, J., & Rowe, C. M. (1985). Statistics for the evaluation and comparison of models. *Journal of Geophysical Research: Oceans*, *90*(C5), 8995–9005. http://dx.doi.org/10.1029/JC090iC05p08995, URL https://onlinelibrary.wiley.com/doi/abs/10.1029/JC090iC05p08995, _eprint: https://agupubs.onlinelibrary.wiley.com/doi/pdf/10.1029/JC090iC05p08995.

Wouters, H., De Ridder, K., Poelmans, L., Willems, P., Brouwers, J., Hosseinzadehtalaei, P., Tabari, H., Vanden Broucke, S., van Lipzig, N. P. M., & Demuzere, M. (2017). Heat stress increase under climate change twice as large in cities as in rural areas: A study for a densely populated midlatitude maritime region. *Geophysical Research Letters*, *44*(17), 8997–9007. http://dx.doi.org/10.1002/2017GL074889, URL https://onlinelibrary.wiley.com/doi/abs/10.1002/2017GL074889, _eprint: https://agupubs.onlinelibrary.wiley.com/doi/pdf/10.1002/2017GL074889.

Yao, L., Sailor, D. J., Yang, X., Xu, G., & Zhao, L. (2023). Are water bodies effective for urban heat mitigation? Evidence from field studies of urban lakes in two humid subtropical cities. *Building and Environment*, *245*, Article 110860. http://dx.doi.org/10.1016/j.buildenv.2023.110860, URL https://www.sciencedirect.com/science/article/pii/S0360132323008879.

Zhao, Y., Chew, L. W., Kubilay, A., & Carmeliet, J. (2020). Isothermal and non-isothermal flow in street canyons: A review from theoretical, experimental and numerical perspectives. *Building and Environment*, *184*, Article 107163. http://dx.doi.org/10.1016/j.buildenv.2020.107163, URL https://www.sciencedirect.com/science/article/pii/S0360132320305370.